2018

Inorganic Nanocrystals And Their Applications In Hybrid 0D:2D Material Optoelectronics

Mathew Kelley
University of South Carolina - Columbia

INORGANIC NANOCRYSTALS AND THEIR APPLICATIONS IN HYBRID 0D:2D MATERIAL OPTOELECTRONICS

by

Mathew Kelley

Bachelor of Science
Appalachian State University, 2016

Submitted in Partial Fulfillment of the Requirements

For the Degree of Master of Science in

Chemistry

College of Arts and Sciences

University of South Carolina

2018

Accepted by:

Andrew B. Greytak, Director of Thesis

MVS Chandrashekhar, Reader

Cheryl L. Addy, Vice Provost and Dean of the Graduate School

DEDICATION

This thesis is dedicated to

My parents, William and Nicole.

ACKNOWLEDGEMENTS

I would like to express my thanks to my advisor, Dr. Andrew Greytak. His insight and guidance during this work has been incredibly helpful.

I would also like to express much gratitude to all members of the Greytak Research Group. Dr. Bobby Barker, Megan Gee, Adam Roberge, Preecha Kittikhunnatham, Fiaz Ahmed, John Dunlap, and Cole Love-Baker were always available to discuss and troubleshoot, and all have been immensely helpful.

Thanks also goes to my co-advisor, Dr. MVS Chandrashekhar and his research student Josh Letton for their collaborative contributions to this work. Both were available for thoughtful discussion and feedback and were incredibly helpful.

I would also like to thank my parents, William and Nicole Kelley.

A sincere and final thank you goes to all educators—both in and outside of academia—that I have had the opportunity to work with. Thank you for your time, patience, and inspiration.

ABSTRACT

Functional nanomaterials have garnered great interest as candidates for use in next-generational optoelectronics such as solar photovoltaics, light-emitting diodes, and photodetectors. Among these low-dimensional materials, hybrid devices employing both 0D and 2D materials are of interest due to exploitation of the favorable characteristics of each component, and performances superior to standalone counterparts are achievable. This thesis is divided into two parts, as follows. The first two chapters will introduce low-dimensional materials and their favorable characteristics; our work on the formation of ligand-exchanged nanocrystal thin films purified by gel-permeation chromatography will also be discussed. In the second component, the formation and study of two hybrid nanocrystal/epitaxial graphene optoelectronic devices will be presented. My work on a standalone epitaxial graphene/silicon carbide ultraviolet photodetector will also be described.

TABLE OF CONTENTS

LIST OF FIGURES

LIST OF ABBREVIATIONS

AC ..... Alternating Current

ATR-FTIR ..... Attenuated Total Reflectance Fourier Transform Infrared

AFM ..... Atomic Force Microscopy

BJT ..... Bipolar Junction Phototransistor

CW ..... Continuous Wave

DC ..... Direct Current

E_F ..... Fermi level

E_G ..... Bandgap

EG ..... Epitaxial Graphene

FET ..... Field-Effect Transistor

g ..... Current Gain

IMPS ..... Intensity Modulated Photocurrent Spectroscopy

IPCE ..... Incident Photon to Current Efficiency

I-V ..... Current-Voltage

LBL ..... Layer-By-Layer

NC ..... Nanocrystal

OA ..... Oleic Acid

ODE 1-octadecene

PbO ..... Lead(II) oxide

PR ..... Precipitation and Redissoution

QD.....Quantum Dot

RC.....Resistor-Capacitor

RPM..... Revolutions Per Minute

SBH..... Schottky Barrier Height

SC..... Schottky Collector

SE..... Schottky Emitter

SEM.....Scanning Electron Microscopy

SPCM.....Scanning Photocurrent Microscopy

$(TMS)_2S$.....bis(trimethylsilyl) sulfide

UPS..... Ultraviolet Photoelectron Spectroscopy

UV..... Ultraviolet

CHAPTER 1: INTRODUCTION

1.1: INTRODUCTION TO LOW-DIMENSIONAL MATERIALS AND HYBRID 0D:2D MATERIAL PHOTODETECTORS

As the spatial dimensions of a material approach the nanoscale, the influence of the size and shape on the material's optical and electronic properties begins to dominate. For crystalline, inorganic semiconductors, the characteristic length scale upon which the material's properties deviate from the bulk is the exciton Bohr radius (a_B). Quantum confinement of electrons and holes occurs when the one of the material's dimensions is reduced to the scale of a_B. From this, three functional nanostructures arise: (1) quantum wells, which are quantum confined in 1 dimension, (2) nanowires, which are quantum confined in 2 dimensions, and (3) quantum dots (QDs), which are quantum confined in 3 dimensions. QDs, nanowires, and quantum wells are commonly denoted as 0D, 1D, and 2D materials, respectively. Among these nanostructures, colloidal semiconductor QDs have garnered great interest as candidates for use optoelectronic devices including next-generational solar cells, light-emitting diodes, and photodetectors. Although other types of QDs—such as epitaxially grown QDs—are of interest, colloidal QDs are a primary component of this work and all references to QDs will signify that the nanocrystals are colloidal and not epitaxial. Much of the interest in QDs stems from two favorable characteristics: the nanocrystals (NCs) are compatible with low-temperature, solution-based synthetic routes, and their optical and electronic properties may be flexibly tuned through systematic control over the NC size and surface chemistry. The potential

for realizing high-performance optoelectronics by exploiting these characteristics is a primary motivating factor behind the advancement of QD solar cells and photodetectors.

A diverse array of 2D materials beyond inorganic semiconductors have also garnered great interest for use in optoelectronics, energy storage, and chemical sensing applications. Transition metal dichalcogenides, mxenes, and atomically thin 2D allotropes (e.g. phosphorene, graphene) are all widely studied classes of 2D materials. Due to the atomically thin or near-atomically thin geometry of these 2D materials, exotic device architectures such as ultrathin van der Waals heterostructures can be realized. Within the rapidly growing catalog of 2D materials, graphene—the prototypical 2D material defined by an atomically thin layer of covalently bound carbon atoms—showcases exceptional mechanical strength, flexibility, and high carrier mobilities. Graphene is a 2D semimetal that exhibits high tunability in the Fermi level (E_F) through doping, application of an electric field, or interband photoexcitations.[1] Despite these appealing characteristics, its responsivity in photodetectors is limited by its high optical transparency. It is from these considerations that the concept of hybrid 0D:2D optoelectronics stems from.

The conception for hybrid 0D:2D optoelectronics arises from harnessing the favorable characteristics of each nanomaterial to yield a device that is superior to a counterpart utilizing the standalone materials. In the context of 0D:2D photodetectors for this work, emphasis will be placed on semiconductor QDs and graphene. Semiconductor QDs are solution processable and do not require extensive growth systems that are required for conventional semiconductors (e.g. silicon) used in commercial optoelectronics. In addition, quantum confinement of the QDs imparts high tunability in

the effective bandgap of the material, making arrayed structures with pixels sensitive to the wavelength regime of interest a possibility. However, assembled films of QDs are poor conductors, and transport is highly dependent on an ensemble of factors including the surface chemistry, uniformity in particle size, and the spacing between adjacent NCs. Graphene, on the other hand, is an excellent conductor and exhibits several favorable characteristics—as mentioned previously—that can complement QDs to form a hybrid structure. Hybrid QD/graphene photodetectors have been reported, but the graphene is often isolated via mechanical exfoliation of graphite. Although mechanically exfoliated graphene often exceeds the favorable characteristics of graphene synthesized in other manners, high throughput fabrication methods are ultimately what is needed to drive the integration of 0D:2D devices towards commercialization. One method of obtaining wafer-scale and uniform graphene is epitaxial growth on silicon carbide (SiC) substrates. SiC is a semiconductor with a bandgap in the ultraviolet (UV). As a result, standalone EG/SiC structures may function as UV photodetectors and have been reported.[2–4] However, the fabrication and characterization of hybrid QD/EG devices is an area left relatively unexplored and is the primary focus of this work..

This thesis is divided into three main areas. Initially, the development of ligand-exchanged PbS QD thin films for hybrid 0D:2D optoelectronics will be described. Then, the fabrication and characterization of two conceived QD/EG photosensors employing two different modes of transport will be presented. Finally, my work on a standalone EG/SiC photosensor for UV detection will be reported.

.

CHAPTER 2: PREPARATION AND CHARACTERIZATION OF PbS QUANTUM DOT THIN FILMS FOR OPTOELECTRONIC DEVICES

2.1: INTRODUCTION

Towards the goal of developing hybrid 0D:2D optoelectronics for light sensing, an initial objective of establishing protocols for the fabrication of ligand-exchanged lead sulfide (PbS) QD films from QDs purified by gel-permeation chromatography (GPC) was identified. We selected PbS over other widely studied semiconductors due to its identical and low bulk effective carrier masses (0.1 m_0 for both the electron and hole, with m_0 being the rest mass of an electron) and a relatively large exciton Bohr radius (a_B = 18 nm); in contrast, the a_B of cadmium selenide and indium phosphide are 4 nm and 8 nm, respectively.[5,6] Arising from the large a_B, size-dependent confinement effects on the optical properties of PbS NCs are observable at relatively larger particle sizes, and the bandgap of PbS QDs is widely tunable and has been reported to span 0.55 to 1.6 eV, which encompasses the entire NIR regime.[7,8] In relation to commercial-scale implementation of PbS QDs in consumer electronics, sulfur also showcases a higher elemental abundance than the heavier chalcogens Se and Te.

Exchanging the native ligands terminating the surface of QDs is a necessary step in the fabrication of NC optoelectronics. Following a typical synthesis, native long-chain organic ligands (e.g. oleate) function to preserve the colloidal stability of the sample and prevent particle aggregation. Upon deposition of the QDs to form a film, the long-chain native ligands function as insulating barriers and diminish the extent of

QD electronic wavefunction interactions needed to achieve high-mobility, delocalized band-like transport.[9] As the interparticle distance between QDs decreases, the wavefunction interaction (i.e. electronic coupling) between neighboring QDs increases, resulting in the formation of bands in an assembled NC solid. Thus, exchanging the population of native, insulating ligands with shorter and/or conductive ligands serves to facilitate charge transport—a desirable characteristic in NC solids. For our films, we chose to exchange native ligands with 1,2-ethanedithiol (EDT) due to its short length[10] (0.41 nm) and capacity to crosslink neighboring QDs; crosslinking is superior and favors the development of relatively longer-range order, which facilitates better charge transport in the assembled film.

We chose GPC as an appropriate purification technique for our PbS samples. Following synthesis, a purification step is undertaken to isolate the sample from reaction byproducts, remnant precursors, and weakly-bound ligands. Most commonly, this purification step is conducted through precipitation and redissolution (PR) cycles employing an antisolvent and solvent, respectively. For QDs suspended in nonpolar solvents such as toluene, agglomeration of QDs is induced by the introduction of a more polar solvent, such as methyl acetate or acetone. The extraneous species that remain dissolved in the liquid phase may then be decanted, and the agglomerated QDs are then redispersed in a nonpolar phase; such PR cycles may induce the loss of native ligands bound to the surface and metal-ligand moieties.[11] The Greytak lab has established the effectiveness of gel permeation chromatography (GPC) as a purification technique in InP, CdSe, and CdSe/$Cd_xZn_{1-x}S$ QD systems.[11] GPC is a form of size exclusion chromatography and operates on the basis of larger particles eluting faster than smaller

particles due to interactions with the stationary phase. A key advantage of using GPC to purify QDs is that the purified sample consists of QDs capped exclusively with strongly-bound ligands, eliminating weakly-bound species that remain even after purification by PR. This is particularly valuable for the assembly of QD thin films for two reasons: (1) the population of strongly-bound ligands at the surface of the purified sample may be quantitatively determined, allowing for direct comparisons between the initial states of samples prior to film formation, and (2) the removal of weakly bound ligands ensures that those species do not interfere with a desired ligand exchange process (i.e. remnant oleic acid does not persist and function as an electrically insulating barrier). Taking all factors into account, we hypothesized that the assembly of ligand-exchanged thin films from QDs purified by GPC held potential to facilitate superior performances in nanocrystal optoelectronics. To my knowledge, the implementation of GPC-purified QDs in thin film optoelectronics had not yet been reported at the time of this work.

In addition to the post-synthetic purification of the QDs, the thickness of our QD films was also taken into consideration. We desired a QD film that was thick enough to absorb incident light and generate a large population of photoexcited carriers, but also thin enough to facilitate charge transfer to contacts interfaced with the film. Thus, a target film thickness of 80-150 nm was chosen based on reported diffusion lengths ($10^1 - 10^2$ nm) of ligand-exchanged PbS and PbSe QD films.[12,13] Because QDs are dispersed in the liquid phase as a colloid, the NCs may be deposited onto a desired substrate by several physical methods such as dip coating, drop casting, or spin coating. For our work, spin coating was identified as the most appropriate technique. Spin coating allows for control over the film thickness by manipulating the substrate rotation speed (**Figure 2.1A**).

Although control over the film thickness may be achieved through dip coating by adjusting the submersion and withdrawal velocities, the technique requires that enough sample is readily available to submerge the substrate used. Because deposition by spin coating is typically conducted with sample volumes on the scale of 1 drop (~50 μL), we considered that the sample volume could be conserved more effectively by spin coating. We note that although long-range order (~1 mm^2) has been reported for drop casted, oleate-terminated PbS QD thin films 1-5 monolayers in thickness, spin coating was deemed more appropriate for this work because the substrate rotation speed functions as an additional parameter for controlling film thicknesses and ligand exchange has been reported for films prepared by spin coating.[14,15] **Figure 2.1B,C** depict the structure of oleic acid and EDT ligands chosen for exchange in our films to yield dense, closely-packed QD solids.

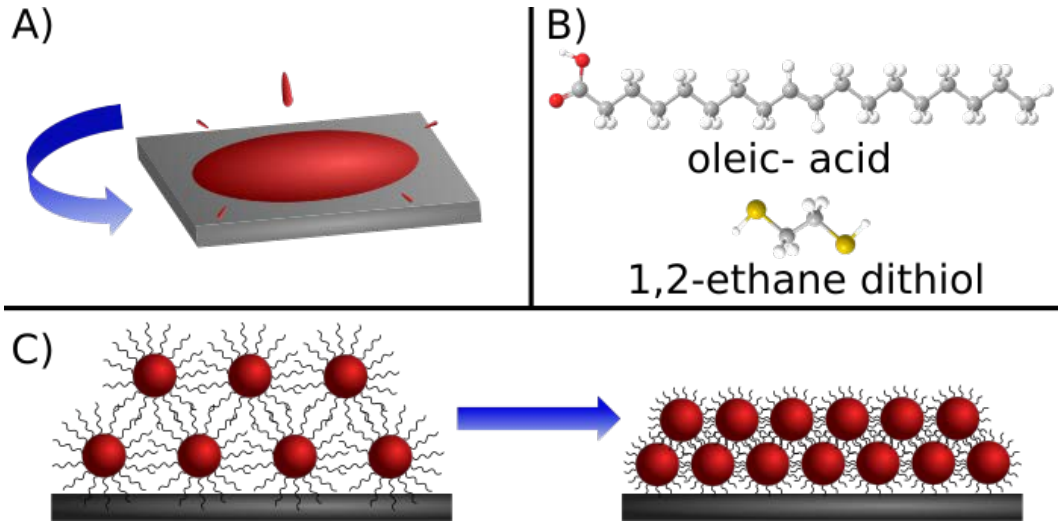

Figure 2.1: Film formation schematic. Panel A displays the spin coating procedure. Protonated forms of ligands bound to the surface of QDs are shown in Panel B; oleate ligands function to maintain the colloidal stability and size of the QDs in solution and are exchanged with shorter ligands such as EDT for thin film electronics. A simplified graphic of the solid-state ligand exchange process is shown C, where exchange occurs on the substrate following deposition.

2.2: NANOCRYSTAL PREPARATION

The colloidal synthetic route described by Luther et al. was used for the preparation of lead sulfide (PbS) QDs due to its capacity for accurately yielding samples with a desired size and effective bandgap.[8] Following synthesis, the samples were subsequently purified by PR and GPC under air-free conditions and dispersed in toluene.[11] Air-free conditions were chosen to facilitate sample consistency from batch-to-batch; exposure to oxygen may cause the formation of surface oxides, which can behave as dopants in an assembled film.[16]

A concentrated sample solution is necessary in spin coating to deposit a sufficient amount of QDs in a layer-by-layer (LBL) process while also reducing the number of steps needed for the desired film. Typically, the concentration of samples post-purification was 5-10 mg/mL, but 20-30 mg/mL or greater was cited in previous reports on LBL assembly by spin coating.[15] Calculation of the sample concentration in mg/mL was as follows. The molar concentration of the purified PbS QDs was determined from a published sizing curve based on the 1S excitonic absorption peak and extinction coefficient at 400 nm; utilization of sizing curves are particularly advantageous over empirically measuring the size of QD samples (e.g. via transmission electron microscopy) because an absorbance measurement does not require as large of an investment in time.[7] The sizing curve was constructed by Moreels et al. from empirical data obtained in transmission electron microscopy measurements on PbS QDs.[7] The expression for estimating the size of the QDs is shown in **Equation 1**, where E_G and d represent the effective bandgap and diameter of the QDs in nanometers, respectively.[7]

The molar concentration of the QDs was obtained from the expression in **Equation 2**, where ε_{400} is the molar extinction coefficient at 400 nm.[8]

$$E_G = 0.41 + \frac{1}{0.252d^2 + 0.283d} \ (Equation\ 1)$$

$$\varepsilon_{400} = (2.3 \cdot 10^4 \times d^3)(Equation\ 2)$$

Following determination of these values, the concentration in mg/mL was determined as follows. QDs were treated as spherical particles with a volume obtained from the diameter in **Equation 1**. The number of PbS unit cells —with a known mass in

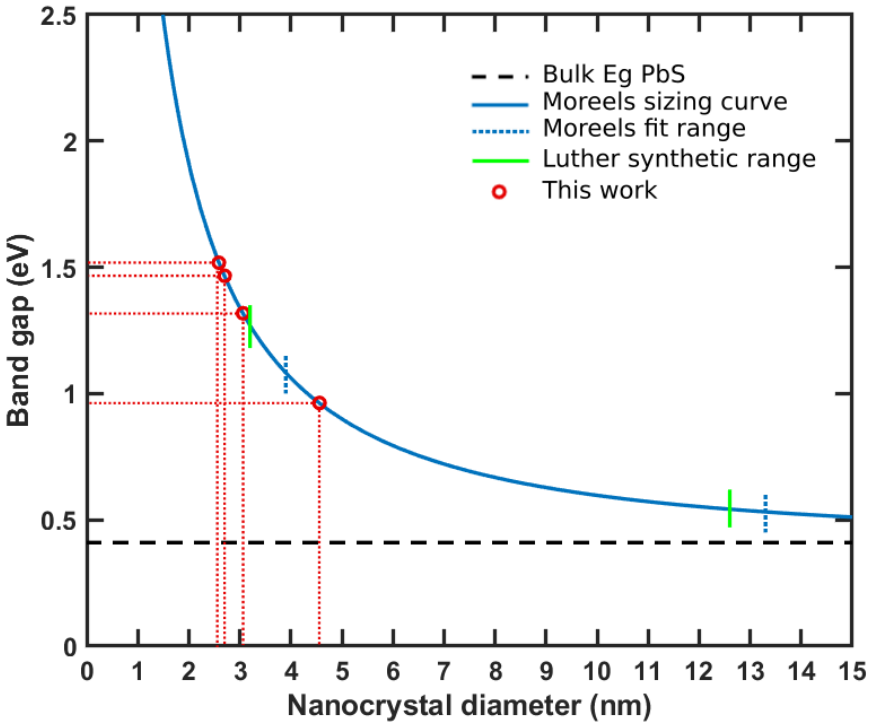

Figure 2.2: PbS Quantum Dot sizing curve. The curve was reported by Moreels et al.[7] and used to estimate the diameter of QDs used in this work. PbS QDs used in this work are designated with red markers; corresponding dotted lines indicate the effective band gap and sizes of the QDs. Blue hashes on the sizing curve indicate the range of QD sizes used to construct it. Green hashes indicate the range of QD sizes obtainable as reported by Luther et al. in the synthetic preparation of the QDs.[8] The black dotted like shows the bulk PbS bandgap energy, which is approached as the QD size nears the exciton Bohr radius.

mg— within that volume was determined based on the lattice parameters of PbS to gain the mass of an individual QD.[5] Finally, the concentration in mg/mL was obtained from the molar concentration of QDs and mass of PbS in the sample. Solvent removal under partial vacuum was used to achieve an estimated sample concentration of 20-30 mg/mL. Normalized absorbance spectra of the dispersed, GPC-purified PbS QDs used for establishing film formation conditions are displayed in **Figure 2.3A**. The 1S excitonic absorbance peaks correspond to effective bandgaps and NC diameters of ~1.5 eV and ~2.8 nm, respectively.

2.3: LIGAND EXCHANGE CHARACTERIZATION BY ATR-FTIR AND SURFACE MORPHOLOGY BY SEM AND AFM

To establish baseline parameters of films prepared from GPC-purified PbS QDs, a series of single-layered, oleate-capped QD films were deposited as a function of substrate rotation speed on Si substrates. In this context, 'single-layered' denotes that a single drop of the oleate-capped QDs were administered to the rotating substrate, and the film was not a monolayer of QDs. The thicknesses of the initial series of films were measured by cross-sectional scanning electron microscopy (SEM). Corresponding data for the single-layer films and are displayed in **Figure 2.3B**. Because it was expected that the film volume would reduce during the ligand-exchange process, an initial substrate spin speed of 2000 rpm was chosen for films treated with EDT.

Two ligand-exchanged films—a single-layer and triple-layer film— were then prepared. Because the formation of non-conductive voids may occur during the ligand-exchange process due to reductions in film volume, examination of the film surface morphology by SEM was also conducted to identify the best candidate for QD/EG

devices. Film thicknesses of the single- and triple-layer EDT-exchanged films are displayed in **Figure 2.3C**. For these initial films deposited at 2000 rpm, large

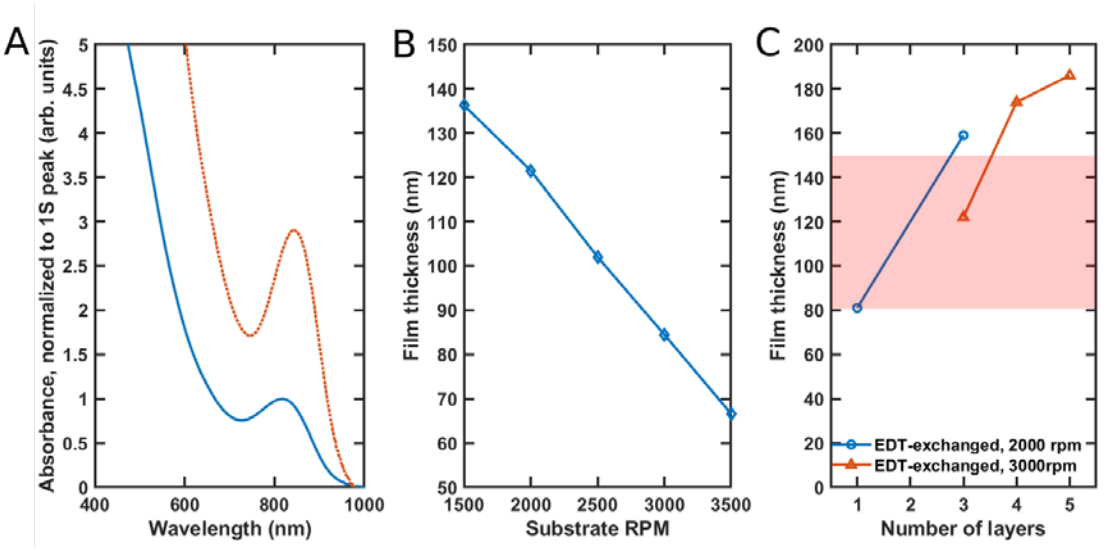

Figure 2.3: QD absorbance spectra and spin curves of PbS QD films. Panel A shows the normalized absorbance spectra of dispersed GPC-purified PbS QDs (E_G ~ 1.5 eV) used in establishing film formation conditions; the spectra have been scaled to distinguish the excitonic 1S peak. Panel B shows the relation between film thickness and spin speed for oleate-capped QDs on Si substrates. Panel C shows the relation between film thickness and spin speed for films deposited in a LBL fashion. The shaded bar indicates the target film thickness of 80-150 nm, which was achieved by the 3x LBL EDT film. All film thicknesses were measured by SEM.

cracks with sizes on the order of 200 nm were observed in the single-layer film, as shown in the SEM micrographs in **Figure 2.4A,B**. At the same spin speed, it was observed that the population and size of voids were much less in the triple-layer film (**Figure 2.4C,D**). The reduction in void severity was due to successive infilling by the additional two QD and ligand exchange steps. Although we noted that the triple-layer EDT-exchanged film held superior surface morphology than the single-layer counterpart, the thickness fell outside of the target range, and a second series of EDT-exchanged thin films was prepared.

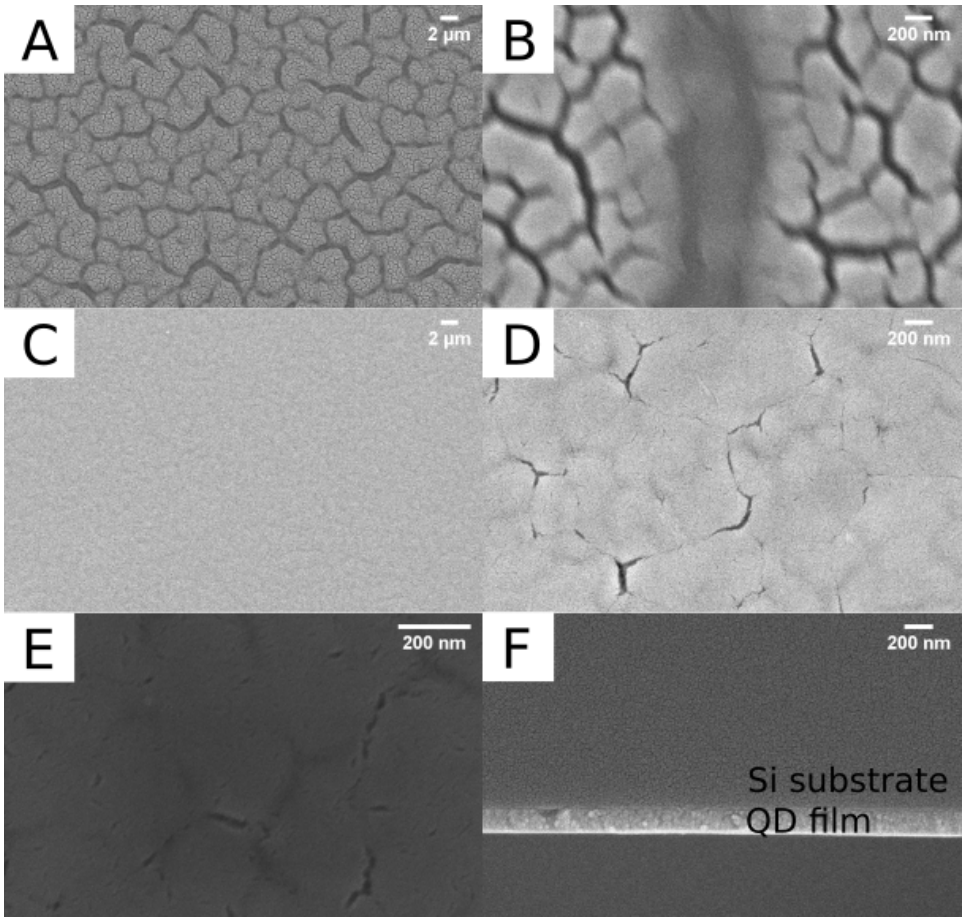

Figure 2.4: SEM images of PbS QD thin films. SEM micrographs of GPC-purified PbS QD (E_G ~ 1.5 eV) films were deposited on Si substrates. Image A shows a representative cross-sectional image of an EDT-exchanged film. Images B,C indicate the reduced cracking in surface morphology of 3x LBL EDT-exchanged films in contrast to the 1x LBL EDT-exchanged film shown in images E,F. Image D shows a comparable surface morphology in a 3x LBL EDT-exchanged film to that of panel C, indicating that successive layer deposition held a greater effect on the surface morphology than substrate spin speed; films in C and D were deposited at 2000 and 3000 rpm, respectively.

EDT-treated films deposited at 3000 rpm for 3-, 4-, and 5-layers all showed comparable surface morphologies to that of the film in **Figure 2.4C,D**; a representative SEM micrograph is displayed in **Figure 2.4E**. The decreasing relative change in film thickness with an increased number of layers (**Figure 2.3C**) suggested infilling of voids by subsequent layers. Of the 3 films, the thickness of the triple-layer exchanged film was

found to fall within the target range and we chose to use it for the investigation of QD/EG devices.

For the PbS films deposited as described in **Figure 2.3**, attenuated total reflection Fourier Transform infrared (ATR-FTIR) spectroscopy was used to evaluate the elimination of oleate ligands from the surface of the PbS film upon treatment with EDT. ATR-FTIR is a common diagnostic technique used in the preparation of QD thin films en route to the fabrication of NC optoelectronics.[17–19] In a 3-layer film prepared without EDT treatment, peaks with wavenumbers of 1520 cm^{-1} and 1396 cm^{-1} were assigned to asymmetric ($\nu_{as}(COO^-)$) and symmetric ($\nu_s(COO^-)$) carboxylate stretches, respectively, corresponding to bidentate bound oleate ligands.[20] Peaks around 3000 cm^{-1} were assigned to alkane/alkene stretches.[20] The absence of a characteristic sharp carbonyl stretch around 1680-1700 cm^{-1} suggested that unbound oleic acid was not present. For an EDT-treated film deposited under the same conditions, the absence of carboxylate stretches suggested that the oleate ligand population had been eliminated.[17] Surprisingly, a lack of aliphatic C-H stretches that would be expected from bound thiolate ligands was observed, although similar results were reported in ATR-FTIR measurements on EDT-exchanged films by Bessonov et al.[19] Further characterization by thermogravimetric analysis or small angle x ray scattering could reveal information on the presence of chemical species and changes in the NC packing density upon ligand exchange, respectively.

Preservation of the excitonic absorbance feature in **Figure 2.4B** indicated that confinement of the QDs was maintained following deposition as a ligand-exchanged thin film. A redshift of 23 nm (39 meV) in the 1S peak was observed; such redshifts may be

due to agglomeration of the QDs during the *in situ* ligand-exchange process. Broadening of the 1S peak half width at half maximum from 104 meV to 185 meV suggested an increase in the size dispersion of the deposited NCs which may have been due to particle agglomeration. We note that an absorbance spectrum for oleate-capped QDs was not obtained, and definitive conclusions concerning particle agglomeration from deposition into a film cannot be fully constructed. However, for the purpose of this work, the EDT-exchanged film was deemed appropriate, given that the film has been cleared of oleate-ligands and retains quantum confinement.

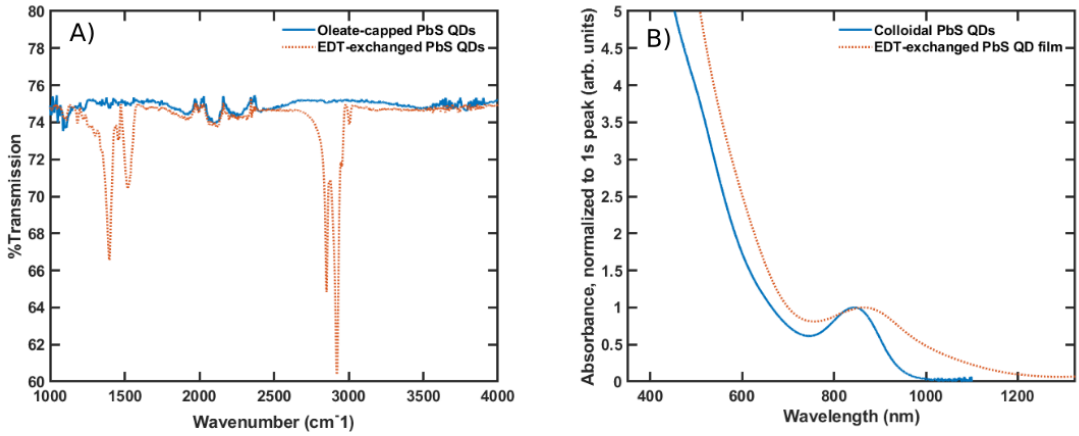

Figure 2.5: ATR-FTIR and absorbance spectra of PbS QD thin films. ATR-FTIR (A) and UV-vis-NIR (B) spectra for PbS QD samples. Panel A indicates the elimination of oleate species from films exchanged with EDT in our LBL process. Panel B indicated retainment of quantum confinement in assembled films of ligand-exchanged PbS QDs.

A film following the general recipe above was deposited on an unetched EG/SiC chip (DH-46) to evaluate whether the film formation would match that of films deposited on Si substrates. Because the size of typical EG/SiC chips were much smaller in area compared to Si chips, the volume of QD sample was reduced from 1 drop (~50 μL) to 15 μL per layer to conserve sample, and a fourth cycle of the LBL QD and ligand exchange process was performed. The film thickness measured from the height contrast between

the EG and the QD film was ~ 149 nm, indicating that the spin coating protocols yielded thinner, but comparable film thicknesses on the EG/SiC substrates. Representative AFM micrographs of bare EG are displayed in **Figure 2.5A,B**. The root mean square (RMS) roughness of blanket EG on SiC and mesa-isolated EG on SiC were 17 nm and 12 nm, respectively. The rough surface stems from the 8° offcut axis of the underlying 4H-SiC substrate. The RMS roughness on the LBL-deposited QD film on the blanket EG chip

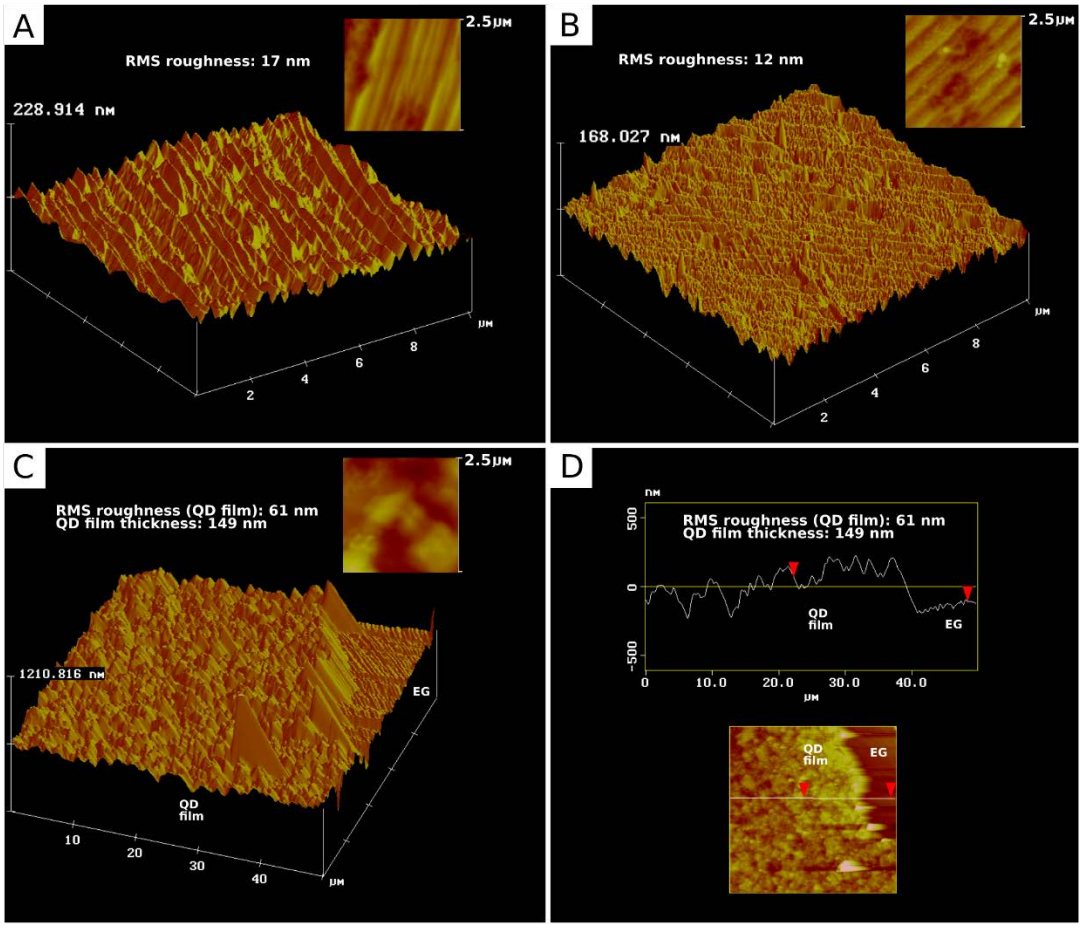

Figure 2.6: Representative AFM micrographs of substrates and PbS QD thin film. Panel A and B show AFM micrographs of a blanket EG chip DH-46 and an EG mesa on chip CL-X3, respectively. Panel C shows a representative AFM micrograph of PbS QDs (E_G ~ 1.3 eV) film spin coated on chip DH-46. Red arrows in panel D indicate a representative profile line trace used to measure the film thickness on DH-46; the corresponding micrograph is indicated in the bottom image of panel D. Insets in panels A-C show a 2.5x2.5µm portion of the respective sample. Vertical axes on isometric micrographs indicate height.

was 61 nm, which was comparable to the RMS roughness of 59 nm obtained from a QD film deposited on a polished Si substrate. Although the thickness of the film was thinner than films deposited on Si substrates, the thickness was comparable and we chose to continue with the established LBL procedure for our prototype QD/EG devices.

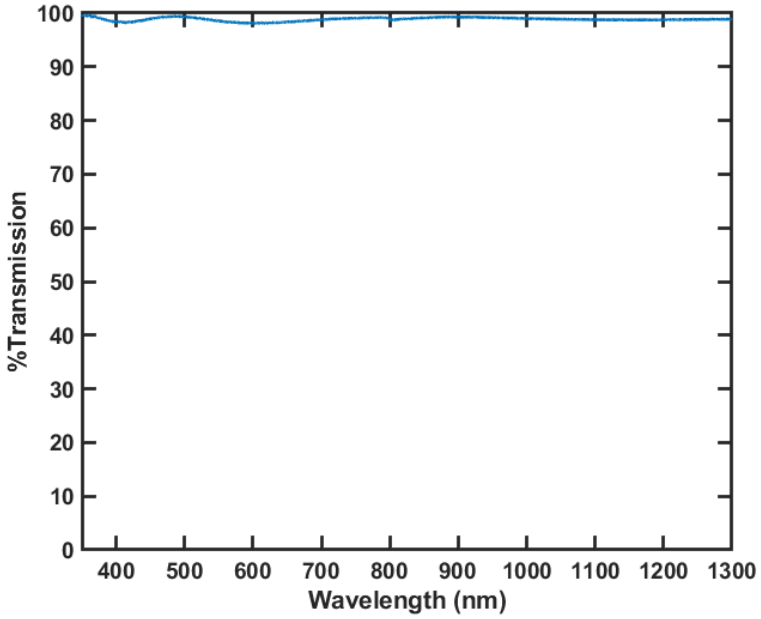

Figure 2.7: Transmittance spectrum of PMMA thin film. The film was deposited on a rotating glass substrate at 3000 rpm. One drop of the dissolved PMMA (MW: 350 K, 2 % (w/w) in anhydrous toluene) was used for the film. The percentage transmittance was found to be greater than 95 % throughout the entire visible region and NIR region of interest.

Finally, transparent polymer layers function as passivating barriers to prevent degradation of the QDs under ambient conditions.[21] PMMA was deemed appropriate due to its high optical transmittance (>90%), ensuring that the polymer layer would not hinder photoexcitation of the QD layer in the wavelength range of interest. A representative percentage transmission spectrum is shown in **Figure 2.7**.

2.4: CONCLUSION:

We have established conditions for preparing QD films suitable for preliminary QD/EG devices and subsequent optoelectronic characterization were established. Thin films of ligand-exchanged, GPC-purified PbS QDs were prepared using a LBL process. Removal of oleate ligands in EDT-treated films was supported by ATR-FTIR, and the preservation of quantum confined NCs was confirmed by absorbance spectroscopy. Multilayer films showed a much lower population of cracks in the surface morphology and were deemed sufficient for prototype QD/EG devices. Further ancillary characterization through thermogravimetric analysis or x-ray scattering could provide a more thorough description of the films following the *in situ* LBL ligand exchange process.

2.5: EXPERIMENTAL

Materials: All reagents were used as received. Lead(ii) oxide (PbO, 99.9 %), anhydrous acetonitrile (ACN, 99.8 %), anhydrous toluene (99.8 %), and 1,2-ethanedithhiol (EDT, 98 %) were purchased from Alfa Aesar. Bis(trimethylsilys) sulfide ($(TMS)_2S$, 95 %) and 1-octadecene (ODE, 90 %) were purchased from Acros Organics. Molecular sieves (4 Angstrom) were purchased from Mallinckrodt and activated by heating under partial vacuum prior to transferring into a nitrogen glovebox. Methyl Acetate (MeOAc, 99 %) was purchased from Millipore Sigma and dried under activated molecular sieves in a nitrogen glovebox following degassing under partial vacuum. Polystyrene Bio Beads (S-X1, 200-400 mesh) were purchased from Biorad. The Bio-Beads were prepared following the procedure by Shen et al with slight modifications, as follows.[11] Toluene was evacuated from the swollen Bio-beads under partial vacuum and

transferred to a glovebox under nitrogen (N2); the Bio-beads were swollen a second time in the glovebox with anhydrous toluene, following the procedure by Shen et al.[11] Poly(methyl methacrylate) (PMMA, 350K) was purchased from Alfa Aesar. The dry PMMA powder was dissolved in anhydrous toluene at a concentration of 2-4 % (w/w) prior to spin coating. Polished Si wafers and glass slides were used as substrates for film samples.

Absorbance Spectroscopy: Routine spectra were collected on a Cary 5000 UV-vis-NIR spectrometer in dual beam mode or a Thermo Scientific Evolution Array UV-vis spectrometer. For samples dispersed in solution, a quartz cuvette with a path length of 10 mm was used. Glass slides were used as substrates on a solid sample holder for measurements on QD films. The film was measured on the Cary 5000 UV-vis-NIR spectrometer because broadening of the 1S absorbance peak extended past the detector cutoff of the Thermo Scientific spectrometer. The lower energy shoulder of the 1S absorbance peak was used for determining half-width at half maximum values.

ATR-FTIR Spectroscopy: A Perkin Elmer Spectrum 100 instrument equipped with a diamond/ZnSe crystal and pressure tower was used for ATR-FTIR measurements. In this context, the 'diamond/ZnSe' refers to a ZnSe crystal under a diamond layer. All samples were measured under ambient conditions.

Synthesis of PbS QDs: PbS QDs were synthesized following the method described by Zhang et al, with slight modifications.[7] In a typical synthesis, PbO (0.225 – 0.45 g), ODE (5 – 10 g), and OA (6 – 8 g) were administered to a 100 mL round bottom flask, stirred, and degassed under vacuum for 20 minutes; ranges specified for reagents were used in accordance to the scale of synthetic batch sizes described by Zhang et al.[8]

The reaction vessel was then heated to 110 ^{o}C under vacuum while stirring to achieve a clear solution, indicative of formation of the Pb(oleate) precursor. The sulfur precursor was prepared by combining ODE (1.25 – 5 mL) and $(TMS)_2S$ (105 – 210 μL). The reaction vessel was then heated to the desired injection temperature (95 – 120 ^{o}C) under positive nitrogen flow, and the sulfur precursor was injected rapidly to the stirring reaction mixture; immediately prior to injection, the heating mantle was removed. The formation of PbS QDs was indicated by the development of a dark brown hue. The reaction mixture was then allowed to cool to room temperature under constant stirring. The sample was then collected for purification.

Purification of PbS QDs by PR and GPC: The collected reaction product was purified by PR under air free conditions with dried MeOAc. The sample was redispersed in anhydrous toluene and then subjected to purification by GPC in a nitrogen glovebox with anhydrous toluene as the mobile phase following the procedure described by Shen et al.[11] A final estimated sample concentration of 20-30 mg/mL in anhydrous toluene was obtained following GPC purification and volume reduction under partial vacuum.

Fabrication of Thin Films by Spin Coating: Polished Si substrates were prepared by cleaving wafers into an area of 1 cm x 1cm. The substrates were cleaned by subsequent submersion cycles (deionized water, acetone, ethanol, acetone) in a bath sonicator and dried under pressurized N_2. All films were deposited in a nitrogen glovebox. Single -layer oleate-capped films were deposited by administering 1 drop of the PbS sample solution to the rotating substrate. Multilayer oleate-capped QD films were deposited in the same manner with the inclusion of a 30 second interval in between each layer to allow for solvent evaporation.

Routine fabrication of films exchanged by EDT was conducted as follows. The substrate was rotated at a constant speed in revolutions per minute (RPM), and a volume of concentrated QD solution was delivered to the rotating substrate. Next, 3 drops of an EDT in acetonitrile (1-3 % v/v) solution was delivered to the substrate. The substrate was then rinsed successively with 2 drops of anhydrous acetonitrile and 2 drops of anhydrous toluene. A hold time of 30 seconds in between each step was permitted to allow residual solvent to dry. This cycle constituted one layer in a typical layer-by-layer (LBL) deposition process.

For thin films deposited on EG/SiC chips, the volume of QD sample was reduced from 1 drop (~50 μL) to 15 μL per layer to conserve sample; the size of a typical EG/SiC chip was much smaller in area than the cleaved Si wafers. Because of this, a fourth cycle of the LBL QD and ligand exchange process was performed. A substrate spin speed of 3000 rpm was used for all films deposited on EG/SiC chips.

Scanning Electron Microscopy: Spin cast films were affixed with carbon tape to standard SEM stumps for examination of cross sectional thickness and surface morphology. In a typical analysis, samples were evacuated and sputtered with Au to facilitate electrical grounding of the samples during measurements. A Zeiss Ultraplus Field Emission SEM was used for all samples.

Atomic Force Microscopy: Samples were measured using a Veeco Nanoscope Dimension 3100 Atomic Force Microscope operated in tapping mode. For film thickness measurements, the sample was scratched with tweezers so that contrast in height between the substrate and film could be obtained. All samples were measured under ambient conditions.

CHAPTER 3: FORMATION OF HYBRID QUANTUM DOT/EPITAXIAL GRAPHENE PHOTOSENSORS FOR VISIBLE AND INFRARED DETECTION

3.1: INTRODUCTION

As noted previously, optoelectronics featuring 2D materials sensitized by 0D nanostructures exploit the favorable properties of each nanomaterial, making the hybrid structure superior to devices employing the standalone materials and conventional alternatives. However, large scale fabrication of 2D materials remains a challenge. For example, reported 0D:2D hybrid devices typically employ 2D materials that have been isolated through mechanical exfoliation, and studies on these systems remains constricted to laboratory prototypes. Among the growing catalog of available 2D materials, epitaxial graphene (EG) grown on silicon carbide (SiC) substrates presents itself as a viable solution toward combating the fabrication bottleneck, as wafer-scale fabrication has been reported.[22] Although standalone EG/SiC phototransistors and photodiodes function well as ultraviolet (UV) photodetectors, the sensing of visible and infrared light by the devices is characteristically impinged by both the low optical absorbance of graphene and the bandgap of SiC, which rests well in the UV.[3,4,23] Here, two conceived hybrid devices utilizing GPC-purified PbS QDs interfaced with EG grown on SiC will be the focus of this chapter. The conception of the devices stems from two literature precedents that featured two distinct modes of electrical transport, as follows: (1) in-plane transport,

wherein photoinduced charge transfer from QDs to a graphene channel resulted in high gain, and (2) vertical transport, wherein molecular adsorption of gases to the surface of graphene in graphene/silicon Schottky diodes resulted in high detection sensitivity at low operating voltages.[15,24] We note that although initial work focused on the in-plane transport of our photovoltage field-effect transistor, our barristor device featuring vertical transport will be discussed first.

3.2: QUANTUM DOT/EPITAXIAL GRAPHENE/SILICON CARBIDE BARRISTOR

Schottky diodes are a type of unipolar device that showcases a rectifying metal:semiconductor junction. For a general Schottky diode, transport across the junction is dominated by thermionic emission theory and follows the current-voltage (I-V) relation in **Equation 3**, as follows.[5,24]

$$I = AA^{*}T^{2}exp\left(\frac{-\Phi_B}{kT}\right)\left[exp\left(\frac{qV}{\eta kT}\right) - 1\right] \ (Equation\ 3)$$

From **Equation 3**, parameters that may be obtained from a I-V measurement include the metal:semiconductor Schottky Barrier Height (SBH, Φ_B) and diode ideality factor (η). Other quantities *A*, *A**, *k*, *q*, and *T* represent the area of the junction, the effective Richardson constant of the semiconductor, the Boltzmann constant, the fundamental electronic charge, and the temperature, respectively. Under reverse bias, the current flow across the junction depends exponentially on the SBH, making it the more favorable operating mode than forward bias where small signals may be less distinguishable from the greater junction current.

Graphene, a 2D semimetal, forms Schottky junctions when interfaced with a semiconductor.[25] The Schottky contact between graphene and the semiconductors has

been reported for graphene grown epitaxially on SiC substrates as well as graphene deposited physically on Si substrates.[2,3,24,25] Although most reported hybrid 0D:2D material photodetectors use modulation of the in-plane conductivity (resistivity) in a 2D material channel, vertical transport in 0D:2D optoelectronics is an area left relatively unexplored, offering the opportunity for a novel device architecture using GPC-purified QDs.

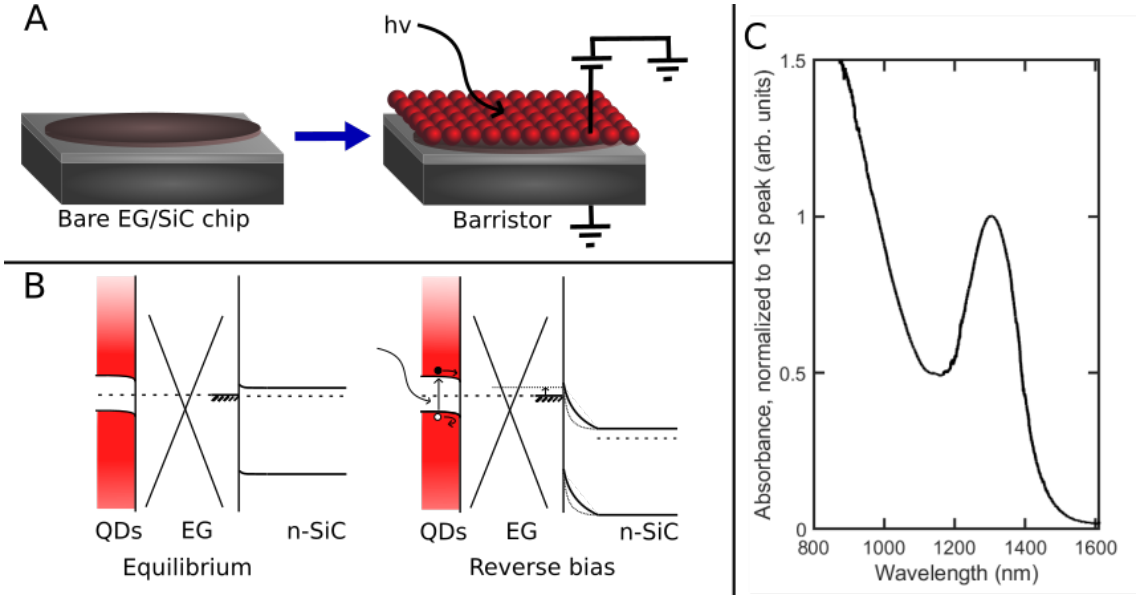

Figure 3.1: QD/EG barristor architecture, operating schematic, and QD absorbance. Device schematic, probing configurations, and proposed energy band diagrams. For clarity, the EG/SiC chip displayed have a single EG mesa; chips used in typical experiments hold several mesa-isolated EG devices for optoelectronic characterization. Panel C shows a representative absorbance spectrum of the dispersed GPC-purified PbS QDs (E_G ~ 0.95 eV) used for the barristor prototype.

Barrier height modulation in vertical graphene/Si Schottky diodes has been the subject of study in chemical sensing. Singh et al. demonstrated that the adsorption of gaseous molecular species on the graphene resulted in modulation of the SBH at the graphene:Si junction, resulting in high sensitivity in the reverse-biased current.[24] For an

EG/SiC Schottky diode interfaced with a visible- or NIR-absorbing QD film, we hypothesized that light sensing could follow a similar mechanism, as follows.

EG/n-SiC Schottky diodes served as the initial platform for our barristor. An illustration of the bare EG/n-SiC chip and envisioned QD/EG/n-SiC device are displayed in **Figure 3.1A**. The prototype device architecture employed mesa-isolated EG interfaced with an n-type 4H-SiC epilayer on a n^+-4H-SiC substrate; further details of the chip are provided in Appendix A. A proposed band diagram of the QD/EG/n-SiC device is shown in **Figure 3.1B**. At thermal equilibrium, the EG/n-SiC junction was anticipated to form a n-type Schottky barrier. The doping of the PbS QD films treated with 1,2-ethanedithiol (EDT) was hypothesized to be p-type and form a p-type Schottky barrier with EG; PbS QD films fabricated in a similar fashion have been reported to demonstrate p-type transport in field-effect transistor measurements.[16,26] It is noted that the E_F of the EG in **Figure 3.1B** rests within the conduction band and reflects n-type doping, which has been shown to occur in EG grown on the Si face of SiC substrates.[27] Upon photoexcitation of the QD film, the diffusion of electrons to the EG layer could result in further n-type doping of the EG and a reduction in the EG/n-SiC SBH, as shown in **Figure 3.1B**. Because of the built-in field at the QD/EG interface, photogenerated holes could remain trapped in the QD film and recombine on a longer timescale than it would take for electrons to traverse the EG/n-SiC barrier, resulting in gain under reverse bias.

An ensemble of preliminary experiments was conducted on EG/SiC chip DH-48 (**Appendix A**) for the barristor prototype. A single EG mesa was selected for all measurements. GPC-purified PbS QDs with an effective bandgap of ~0.95 eV were used for the prototype device; a representative absorbance spectrum of the dispersed QDs is

displayed in **Figure 3.1C**. Chip characterization before and after the application of QDs was conducted as follows. Initially, the reverse and forward biased dark I-V characteristic (**Figure 3.2A,B**) of the device were measured to obtain the ground state EG/n-SiC SBH. Given that the reported values of the electron affinity (X) of n-type 4H SiC is ~3.17 eV and workfunction of EG is ~ 4.5 eV, a SBH of ~1.33 eV was expected.[24,28] Through analysis of the dark I-V characteristics by thermionic emission theory, the EG/n-SiC SBHs were 0.8009 eV and 0.6149 eV for pre and post-QD states, respectively. All extracted diode parameters are displayed in **Table 1**. The data suggest that the SBH was lowered following the application of QDs. Following thermionic emission theory, such a

Table 3.1: Diode parameters for chip DH-48, pre- and post-QDs under dark conditions

	Pre-QDs, dark	Post-QDs, dark
SBH	0.8009 eV	0.6149 eV
I_S	0.2398 nA	0.3159 μA

decrease in the SBH would translate to an enhanced dark current under reverse bias. We found that the reverse-biased dark current was elevated, as shown in **Figure 3.2C,D**. Although the reverse bias dark current in a Schottky diode is not expected to depend strongly on the magnitude of the applied voltage and saturate according to the I_S, we found that the current under dark conditions increased with increasing voltage. Such monotonic behavior has been reported in other graphene:semiconductor Schottky diodes and could be attributed to modification of the SBH caused by changes in the EG work function.[24] Direct measurement of the band offsets and E_F of the QD film, EG, and n-SiC epilayer by Ultraviolet Photoelectron Spectroscopy (UPS) would be valuable in building a working hypothesis for the device operating mechanism. Probing the I-V characteristic of the QD/EG junction would also indicate if transport is Ohmic or rectifying—among

other properties of the junction such as the depletion width— due to a built-in potential; such an experiment would complement band offsets obtained by UPS. Due to the low resolution of the measurements in **Figure 3.2A,B**, the same I-V experiment will be undertaken on future devices at higher resolution to verify the effect of the QDs on the SBH and build upon our device operating mechanism.

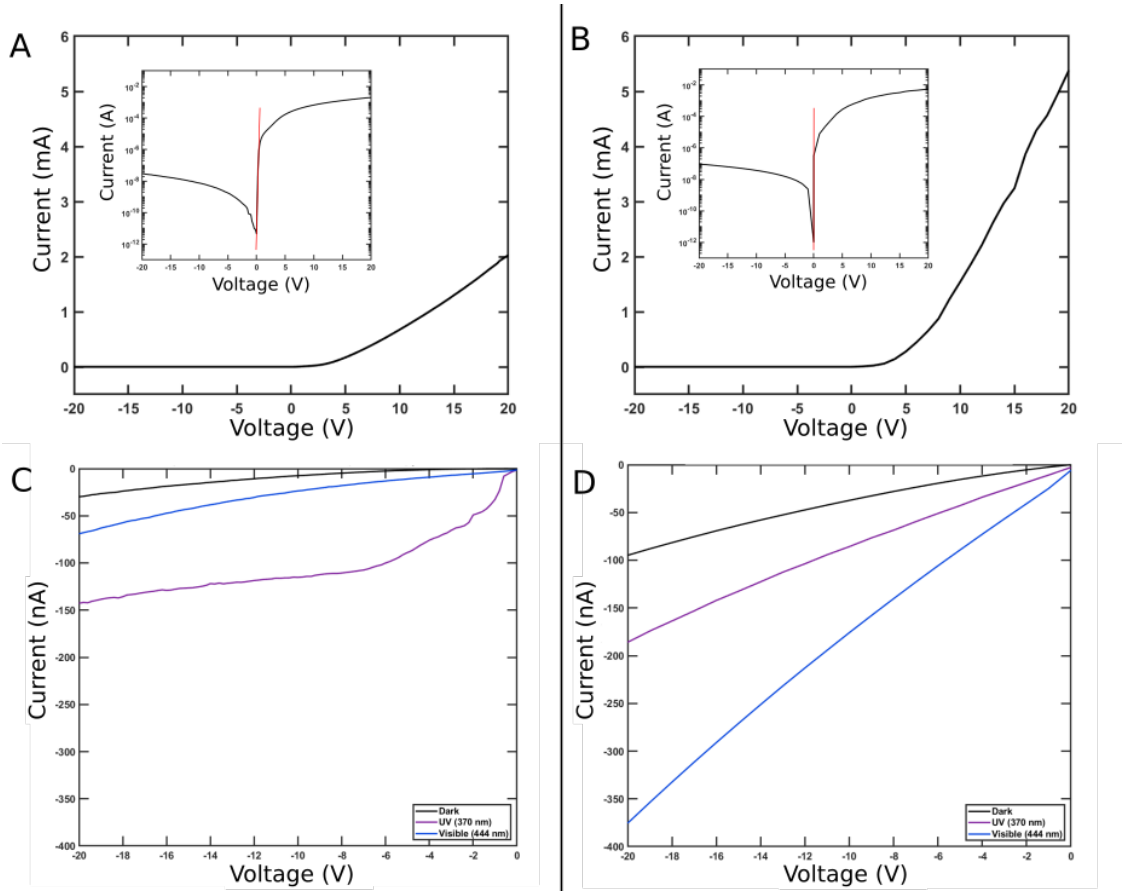

Figure 3.2: QD/EG barristor I-V characteristics. EG/n-SiC/n^+SiC chip DH-48 was used. Left and right panels correspond to measurements taken before and after the deposition of PbS QDs (E_G ~ 0.95 eV/1298 nm), respectively. Panels A and B represent the dark current I-V characteristics; insets show semilogarithmic plots, with the red lines indicating the forward biased linear regions (0-1 V) used for the extrapolation of diode parameters. Panels C and D represent the visible (444 nm) and UV (370 nm) reverse biased I-V characteristics under wide area illumination, respectively. The reverse bias dark current is also displayed. For the data in panel C, illumination powers for UV and visible excitation were 13.8 μW and 392 μW, respectively. For the data in panel D, illumination powers for UV and visible excitation were 8.15 μW and 1.59 mW, respectively.

The reversed-biased I-V characteristics under wide-area visible (444 nm) and UV (370) nm illumination are displayed in **Figure 3.2C,D**. The visible DC (i.e. steady state illumination) responsivities before and after QDs were 9.98×10^{-5} A/W and 1.76×10^{-4} A/W, respectively. UV DC responsivities before and after QDs were 8.18×10^{-3} A/W and 1.12×10^{-2} A/W, respectively. These responsivities were obtained from the I-V curves in **Figure 3.2C,D** at 20 V bias. For both visible and UV excitation, the responsivity increased following QD deposition. Our I-V results confirm that the QDs enhanced the performance of the device under visible and UV excitation, albeit slightly.

To further probe the origin of the enhanced reversed-biased responsivity following the application of QDs, scanning photocurrent microscopy (SPCM) experiments were undertaken. SPCM is a powerful technique that may be used to resolve spatial photocurrent responses and obtain length scales of transport in optoelectronics. All AC photocurrent maps, as well as a representative reflected light map, are displayed in **Figure 3.3**. In this context, AC denotes photocurrent arising from a modulated illumination source. The map of the bare device under visible excitation revealed a highly localized response within the EG mesa, as shown in **Figure 3.3A**. Prior to the application of QDs, transport across the junction under reverse bias was expected to be dominated by the emission of electrons from the EG to the n-SiC. The visible response may have been due to sub-bandgap excitation of the n-SiC epilayer, wherein diffusion of photoexcited holes to the EG contact occur prior to recombination. The absence of a photocurrent outside of the EG mesa suggest that photoexcited carriers are unable to transit the distance to the EG contact before recombining. We attributed the low signal

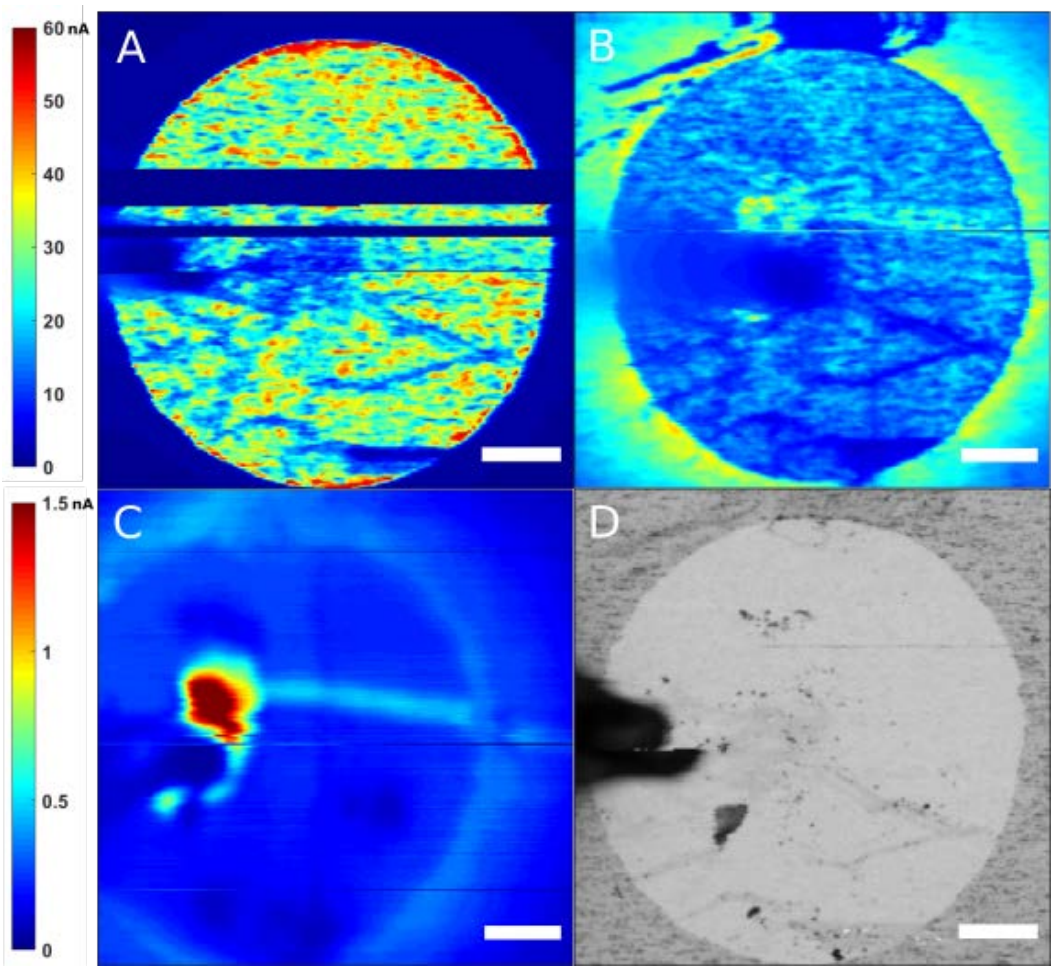

Figure 3.3: QD/EG barristor AC photocurrent maps. All maps were taken on EG/n-SiC/n^+-SiC chip DH-48 under 10 V reverse bias. The top intensity bar corresponds to panels A and B; the bottom intensity bar corresponds to panel C. Panel A and B show the AC visible (444 nm) photocurrent map of the device before and after QD deposition, respectively. Panel C shows the post-QD UV AC photocurrent map.

within the mesa—signified by the sharp, horizontal bar in **Figure 3.3A—**to a temporary loss of contact with the probe during raster-scanning of the microscope stage.

We report a distinguishing feature between maps taken of the device before and after QD deposition: an elevated photocurrent and accompanying decay of signal beyond the edge of the EG mesa was observed for visible and UV AC photocurrent maps taken after the application of the QDs, as shown in **Figure 3.2B,C**. This could be due to in-

plane conduction in the QD film following local excitation at the QD/n-SiC interface, wherein separation of photoexcited carriers occurs most frequently near the mesa and decays further away as recombination occurs prior to collection at the EG contact. Under such a process, transport may be limited by the conductivity of the QD film.

Due to the nature of the SPCM measurement, localized excitation is induced with a focused beam and high power density relative to measurements with a defocused beam. Two features with elevated signals within the EG mesa on the UV SPCM map arose due to photodamage to the QD film. The 1.5 nA feature was due to abrasion of the QD film during contact with the tungsten probe, and the broad 0.5 nA feature was also due to slight abrasion of the film. The low signal within the region of the mesa signified by a narrow vertical line in both post-QD AC photocurrent maps was also due to damage induced by the illumination sources. We emphasize that while the AC photocurrent maps provided spatial origins on the photocurrent of our device, the damages to the QD film may perturb the signals such that quantitative evaluation of the SPCM data is limited.

Per our hypothesis for photoinduced charge transfer, we anticipated a relatively greater response within the region of the EG mesa relative to the surrounding SiC epilayer. However, the responsivity within the mesa under visible excitation was lower in the post-QD experiment than in the pre-QD experiment. Estimated average visible responsivities within the mesa before and after QD deposition were 1.59×10^{-4} A/W and 1.69×10^{-5} A/W, respectively. It is possible that the QD film functioned as a strict filter with no charge transfer effects described in our hypothesis. This behavior would support the attenuation of the responsivity within the mesa following deposition of the QDs.

To obtain a clearer description of the device performance, intensity modulated photocurrent spectroscopy (IMPS) experiments were undertaken under wide area visible and UV excitation. We chose wide area illumination to maximize the area of excitation in

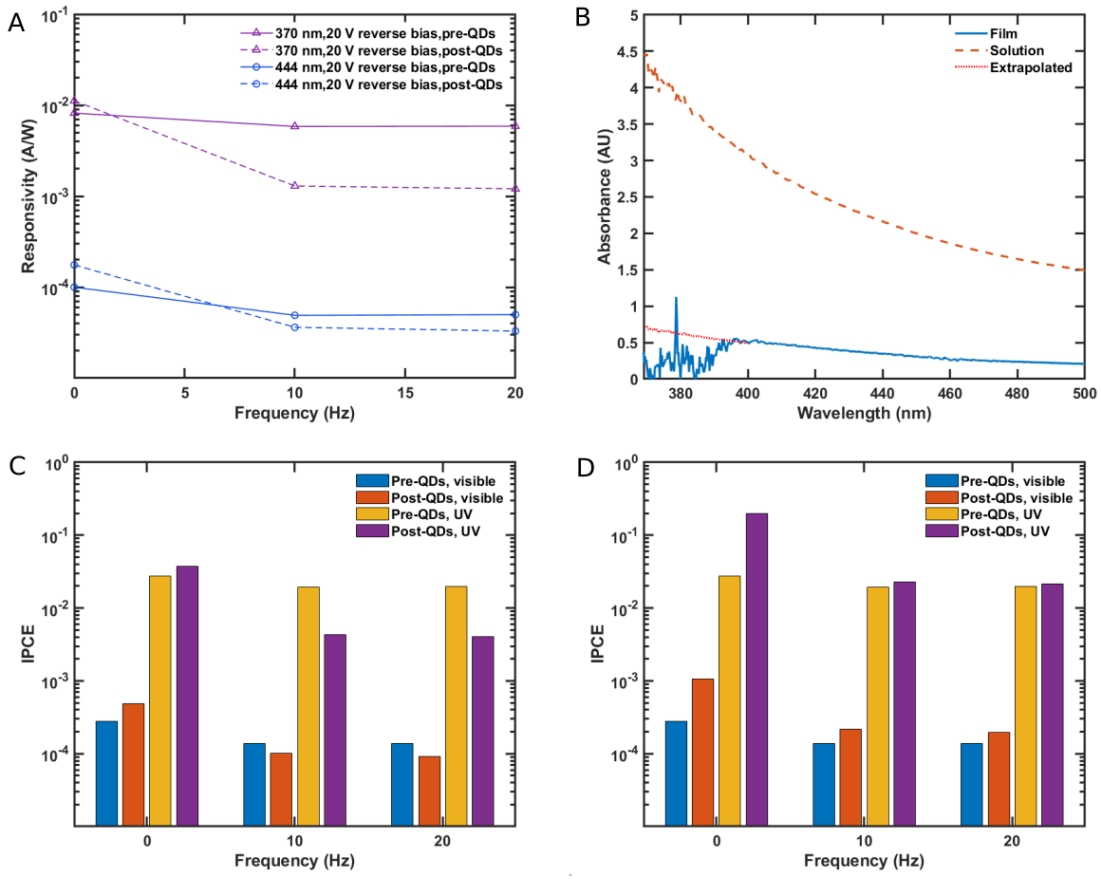

Figure 3.4: Bode plot, QD absorbance spectra, and IPCE. Panel A shows a condensed Bode plot of wide-illumination (~49000 μm^2) IMPS measurements on sample DH-48. Panel B displays the absorbance spectra of the PbS QDs in solution and deposited as a thin film on chip DH-48. The red line indicates the extrapolated region of the film absorbance spectrum used to estimate the absorbance at 370 nm. Panels C shows the IPCE of the device when compared to unity gain of the total incident light, and Panel D shows the IPCE when taking into account treatment of the QD film strictly as an absorptive filter of the incident light.

order to obtain the largest measurable signal. A summary of IMPS measurements under wide area illumination is displayed in **Figure 3.4A**. Attenuation of the device responsivity was observed for pre- and post-QD measurements under both UV and

visible excitation. Modulation of the incident light at frequencies up to 400 Hz did not yield further attenuation of the isolated AC photocurrent signal. We found that the responsivity was attenuated more strongly at low frequency (≤ 10 Hz) modulation following QD deposition than in the bare device. Although the UV and visible photocurrent maps in **Figure 3.3B,C** indicated an enhanced signal following QD deposition at the edge of the EG mesa, the increased responsivity at DC was not be solely attributed to that because all IMPS measurements were taken under wide area illumination. Because the separation of illumination on and off the mesa was not precisely defined in these wide area measurements, the obtained responsivities convolve photocurrent from illumination in regions within the mesa, on the edge, and outside of the edge of the mesa.

Given the enhanced photocurrent at and beyond the edge of the EG mesa in addition to the attenuated signal within the EG mesa following QD deposition, the incident photon to current efficiency (IPCE) of the device was evaluated to better understand the device enhancement imparted from the application of QDs. We considered two conditions: for evaluating the IPCE (1) comparison of the device responsivity to what would be expected from unity gain (1 electron/incident photon), and (2) comparison of the device responsivity to what would be expected from unity gain, while treating the QD film as a strict filter for incident light with no charge transfer effects. For treatment of the QD film as a filter, the 46 % transmittance of the QD film (**Figure 3.4B**) at 444 nm was used to determine an effective optical intensity transmitted through the film and incident with the underlying EG/n-SiC. Extrapolation of the film absorbance spectrum form the spectrum obtained in solution (**Figure 3.4B**) provided an

effective transmittance of 19 % for 370 nm excitation. As shown in **Figure 3.4C,D**, we observed that in both conditions (i.e. QD as a strict filter vs. total incident photons), the IPCE of the device increased for both visible and UV excitation at DC following QD deposition, indicating that enhancement of the device performance stemmed from the presence of the QDs. We also report that although the IPCE was attenuated between pre- and post QD states at frequencies of 10 Hz and greater when considering the total incident photons, the IPCE was enhanced when considering the fraction of incident photons transmitted through the QD film. This indicates that the QDs did enhance the device, although the gain of the device was less than 1 electron /photon. The attenuation of the device responsivity at low frequency (<10 Hz) could arise from several factors, but the exact origin is not known.

3.3: PHOTOVOLTAGE FIELD-EFFECT TRANSISTOR WITH EPITAXIAL GRAPHENE CHANNEL

In contrast to vertical transport in the barristor, our hypothesis for the QD/EG photovoltage field-effect transistor (FET) focused on in-plane transport in an EG channel grown on SiC substrates. In brief, FETs contain three electrical terminals denoted as the drain, source, and gate. The conductivity between the drain and source terminals is modulated by the application of an electric field from the gate terminal. For our envisioned QD/EG photovoltage field-effect transistor (**Figure 3.5A**), two electrical contacts on a single EG mesa served as the drain and source terminals, and a bottom contact to the SiC substrate served as the gate terminal. We hypothesized that QDs deposited on the EG would function as the light absorbing component that would facilitate selective photoinduced charge transfer to the EG, modifying the Fermi level of

the EG and the in-plane resistance of the EG channel. The built-in field at the QD/graphene interface determines whether photogenerated electrons (holes) migrate to the high-mobility channel and holes (electrons) remain trapped in the QD layer. Following charge transfer, the migrated carrier may drift under a bias voltage at the drain terminal and circulate the channel multiple times before recombining, yielding current gain (g) as described in **Equation 4**.

$$g = \frac{\tau_{lifetime}}{\tau_{transit}} \ (Equation\ 4)$$

In **Equation 4**, $\tau_{lifetime}$ and $\tau_{transit}$ represent the lifetime of the trapped carrier and the transit time of the migrated carrier, respectively. This relation shows that high current gain may be achieved in devices where a high carrier lifetime and/or low transit time are present.

The resulting signal stemming from the photoinduced charge transfer to the graphene may be maximized by maximizing the change in channel resistance relative to the dark resistance ($\Delta R/R$); this may be achieved through application of a gate voltage to the graphene such that the Fermi level rests at the Dirac point, or point of greatest resistance. Similar hybrid QD/graphene field-effect transistors utilizing mechanically exfoliated graphene and PbS QDs on SiO2/Si substrates have been reported to demonstrate high gain on the order of 10^8 electrons per photon.[15]

On the same basis as the barristor, hybrid 0D:2D material optoelectronics employing EG/SiC are advantageous over devices employing mechanically exfoliated 2D materials for several reasons, including compatibility with wafer scale fabrication protocols and inherently intimate contact with the underlying SiC substrate. SiC substrates are also advantageous for visible and NIR photodetection in that they are

optically transparent to visible and NIR light, making backside illumination a possibility in hybrid QD/EG/SiC devices. Although top-gated EG/SiC phototransistors sensitized by semiconductor nanostructures have been reported[29], bottom-gated counterparts are an area left unexplored. Bottom-gated devices are potentially advantageous in that the subsequent fabrication steps used to deposit the top gate are no longer required.

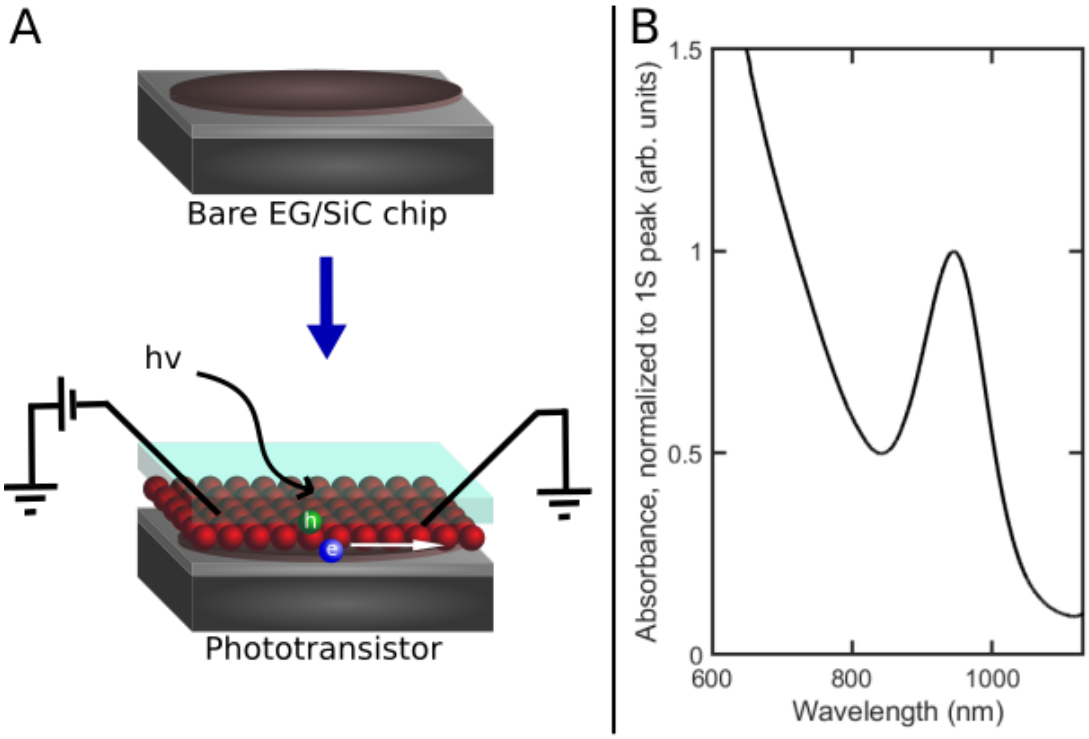

Figure 3.5: QD/EG phototransistor architecture and QD absorbance. The conceived photovoltage field-effect transistor is shown in Panel A. Migrated electrons are shown to transit the EG channel while the trapped holes remain in the QD layer. For clarity, the EG/SiC chip displayed has one EG mesa; chips used in typical experiments hold several mesa-isolated EG devices for optoelectronic characterization. Panel B shows the absorbance spectrum of dispersed GPC-purified PbS QDs (E_G = ~ 1.3 eV) used for this device.

For our prototype photovoltage FET, EG/n-SiC/n^+-SiC chip CL-X3 (**Appendix A**) was used. Initially, we chose to investigate whether the EG channel would demonstrate a change in resistance upon application of a bottom-gate voltage. Because

the EG/n-SiC junction forms an n-type Schottky barrier, gate voltages were applied such that the junction was held under reverse bias; forward bias would have resulted in forward conduction and convolve with the current in the EG channel. We found that the EG channel resistance was consistent at ~10^3 Ω for gate voltages up to 20 V and concluded that the EG did not demonstrate an appreciable gate response that would be suitable for maximizing a ΔR/R.

Because the device did not demonstrate a gate response, two experiments—AC photocurrent and AC photoconductance—were undertaken to more directly probe lateral transport before and after QD deposition. Here, the AC photocurrent experiment will be described first. In this context, AC denotes modulation of the 444 nm illumination beam at a specified frequency. We note that the illumination for these measurements was contained within the EG mesa and to a circular area with a diameter of ~94 μm. The measurement was obtained by applying a 100 mV bias to the drain terminal with the source terminal connected to a current preamplifier and lock-in amplifier referenced to the beam modulation frequency. It was expected that if our device functioned as hypothesized and charge transfer occurred upon illumination, the AC photocurrent would be greater following deposition of the QDs. Two EG mesas—labeled 'Device A' and 'Device B' were measured before and after QD deposition; both devices were circular EG mesas with a diameter of 250 μm. A summary of the AC photocurrent measurements is displayed in **Figure 3.6**. We found that the responsivity and AC photocurrent decreased for both of the tested devices following deposition of the QD film. It is possible that the AC photocurrent originated from absorption in the EG/n-SiC junction, and current obtained was conduction through the gate; such an explanation is plausible

because the measurement did not distinguish in-plane transport and gate conduction. The reduction in photocurrent in the post-QD measurements may have occurred because the NC film functioned as a strict filter without charge transfer effects. With these considerations, the second experiment was undertaken as follows.

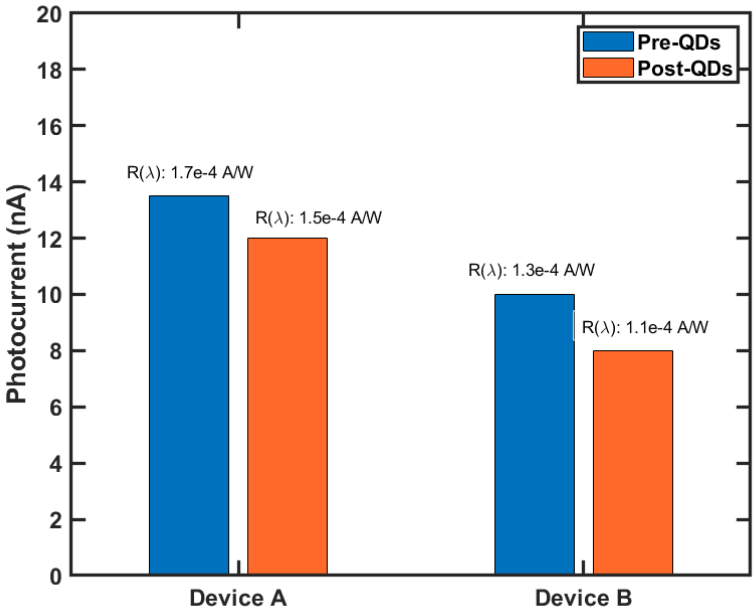

Figure 3.6: AC photocurrent with visible illumination. All measurements were obtained under 444 nm (continuous wave power of 168.3 μW) illumination chopped at a frequency of 37 Hz.

To directly probe changes in the EG before and after QD deposition, an AC photoconductance experiment was undertaken, with a dual lock-in setup. The measurement utilized two excitation sources: (1) AC modulation of the drain voltage at high frequency (1 kHz) on a DC bias, and (2) modulation of the illumination source at a low frequency (37 Hz). We note that the device under test was subjected to both excitations at the same time. The entire signal was passed to the first lock-in amplifier referenced to the frequency of the AC voltage; this served to ensure that gate conduction

was not convolved with current in the EG channel because current not arising from the AC voltage frequency would be eliminated. The output of the first lock-in amplifier was proportional to the conductance of the EG channel. The outbound signal was then passed from the first lock-in amplifier to the second lock-in amplifier referenced to the illumination frequency; output of the second lock-in amplifier was proportional to the photoconductance of the EG channel. It was expected that the photoconductance would increase following QD deposition. A summary of the AC photoconductance measurements is displayed in **Figure 3.7**. We found that for device A, the

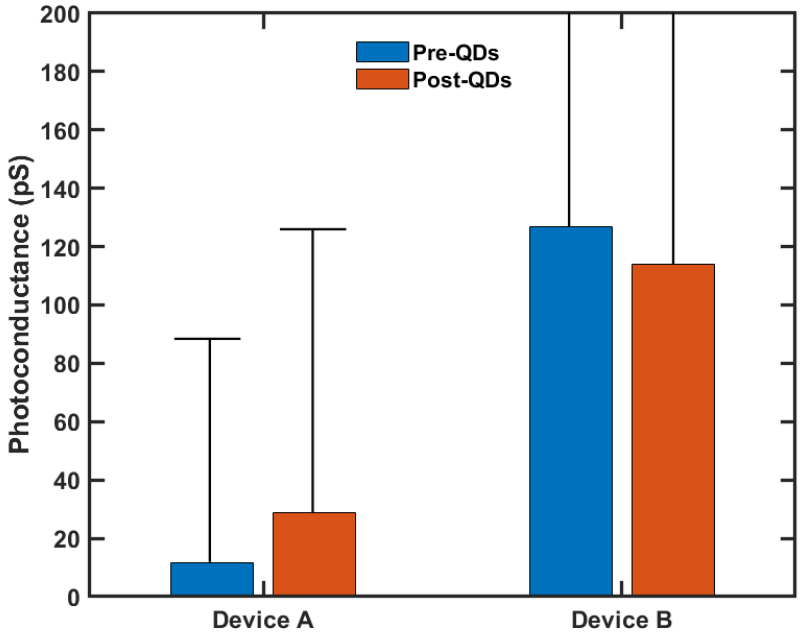

Figure 3.7: AC photoconductance with visible illumination. Vertical bars indicate the standard deviation of the obtained photoconductance signal, recorded over an interval of 20 seconds.

photoconductance increased following the deposition of QDs, but in device B, the photoconductance decreased. The vertical bars indicate the standard deviation of the photoconductance signal, which was recorded over a time interval of 20 seconds. We

note that the standard deviations are large and approached or exceeded photoconductance values. This could be explained from the presence of a small signal on large background noise during the measurement, suggesting that any changes in the EG photoconductance were not large enough to surpass the background. We concluded that the device did not demonstrate enhancement by the QDs, although top-gated devices employing a ionic gel dieletric could serve as an alternative avenue for gated EG photosensors.

3.4: CONCLUSION

We have found that the UV and visible responsivities of an EG/n-SiC Schottky diode was enhanced upon application of a PbS QD thin film. A definitive mechanism of the enhancement is not known, but AC photocurrent maps indicated that the device response is much greater on the outer edge of the mesa and decays from as the distance from the mesa increases. Although the responsivities in the post-QD state were attenuated more strongly than the pre-QD state at low frequency (10 Hz), the IPCE was found to increase when treating the QD film as a strict filter of incident light. We found that the IPCE at DC increased regardless of considering the QD film as a strict filter or accounting for the total incident photons. Further experiments will be obtained to elucidate the enhanced response at the edge of the EG mesa.

To better understand the effects of the QDs on ground state transport, high-resolution I-Vs will be acquired to determine changes in the EG/n-SiC SBH in the ground state. In addition, direct measurement of the QD film E_F and band energy levels will be valuable in constructing a working description of the device band offsets and operating mechanism, in addition to electrical characterization of the QD/EG junction.

For the photovoltage FET, a measurable AC photocurrent was measured, but because the conductance of the EG did not demonstrate a significant change upon illumination, it was concluded that the enhanced photocurrent signal arose from photoinduced current in the EG/SiC substrate and the QDs did not demonstrate an effect on the EG channel. This may have originated from a few factors, as follows. We note that the thickness of the EG was 13-15 monolayers, which is much thicker than the monolayer graphene used in literature precedents. The EG may have been too thick to properly gate, meaning that the maximum $\Delta R/R$ was not able to be controlled by application of a gate voltage. Because the gain in these devices is dependent on the carrier lifetime and carrier transit time, it is possible that excitation did occur in the QDs, but recombination occurred prior to charge transfer to the EG.

3.5: EXPERIMENTAL

Materials: All chemicals were obtained as indicated in previous chapters.

Device Fabrication EG/SiC chips were fabricated using a published procedure.[3] Individual EG/SiC devices were defined by reactive ion etching of the grown EG film, yielding EG mesas. All EG/SiC chips were rinsed with deionized water, acetone, and ethanol prior to testing and the application of QDs. Tabulated chip IDs and sample information are in **Appendix A**. Preparation of the QD film for the preliminary barristor was as follows. On EG/SiC chip DH-48, the EDT-spin-coating procedure described in Chapter 2 was used, with slight modifications. A 20 mg/mL PbS QD (E_G ~ 0.96 eV/1290 nm) solution was administered at a volume of 25 μL for 3 cycles of the EDT ligand exchange process. A passivating PMMA layer was not deposited on the barristor device prototype.

Preparation of the QD film for the preliminary phototransistor was as follows. On EG/SiC chip CL-X3, the EDT spin coating procedure was the same as that used for chip DH-46. Because the same PbS QD sample and spin coating procedure was used, the thickness of the film was estimated to be ~149 nm. Following the QD film, a 90 nm thick layer (as measured by profilometry) of PMMA (2% in toluene (w/w)) was spin coated onto the NCs to function as a passivating layer to prevent degradation of the QDs under ambient conditions.

I-V characteristic: Routine I-V measurements were taken using a Keithley 2636A Source Meter Unit. EG/SiC chip DH-48 was used for the barristor. Electrical contacts were made with a tungsten probe on the EG mesa under test, and Cu tape affixed to the bottom of the chip. For determination of the SBH at the EG/n-SiC junction, the linear region was defined as 0-1V forward bias for both pre- and post-QD dark I-Vs. The effective Richardson constant (A*) was defined as 146 $A/cm^2 \cdot K^2$ for n-type 4H-SiC.[30]

For the phototransistor prototype, electrical contacts were made in the same fashion as that of the barristor except an additional tungsten probe was held in contact with the EG mesa under test. For illuminated measurements, the illumination area was defined by a 20X objective lens (Mitutoyo) with a numerical aperture of 0.42. For measurements taken under wide area illumination, an area of ~49000 μm^2 was used.

EG/SiC sample CL-X3 was used for the phototransistor prototype. Source and drain terminals were defined by contact to the EG mesa with two tungsten probes, with a back contact to the substrate with copper tape functioning as the gate terminal.

SPCM: Measurements were acquired following the procedure described by Barker et al.[2] For visible (444 nm) and UV (370 nm) illumination, the incident beam was

modulated by a mechanical chopper set to 113 Hz. The EG device under test was contacted directly by a tungsten probe, with a back contact defined by copper tape. A constant reverse bias DC voltage of 10 V was applied to the EG mesa. The photocurrent signal was isolated by an Ithaco 1211 current preamplifier and SRS S830 lock-in amplifier. An area of ~300 x 300 μm defined the photocurrent map size, with a resolution of 1 μm^2/pixel. Data was acquired by an in-house developed Labview program.

Calculation of the RMS Optical Power: Several measurements implemented modulation of the illumination beam and isolation of the desired signal through a lock-in amplifier, which delivers the rms amplitude of the input from the reference frequency. Modulation of our illumination sources yields a square wave as the input reference waveform, of which the rms amplitude is obtained by scaling the continuous wave (CW) optical power by a factor of 0.45 (from $\sqrt{2}/\pi$). This rms optical power was used in all calculations of device responsivities in IMPS and AC photocurrent experiments. An example calculation for determining the responsivity from IMPS experiments is presented described as follows. Our measurements used a SRS 830 model lock-in (LI) amplifier, which provides the rms amplitude of the signal on a 10 V scale. The preamplifier (pre) gain was also taken in to account in determining the responsivity, as shown below.

$$R(\lambda) = \left(\frac{LI\ output * LI\ sensitivity\ (V)}{10V}\right)\left(pre\ gain\left(\frac{A}{V}\right)\right)\left(\frac{1}{0.45 * CW\ optical\ power}\right)$$

IMPS: The device under test was illuminated such that the entire EG mesa was held incident with the light beam. The beam was modulated by a mechanical chopper at a frequency of 113 Hz. The device was held at a constant bias by a Keithley 2636A Source

Meter Unit. The modulated photocurrent signal was delivered to an Ithaco 1211 current preamplifier and Stanford Research Systems SR830 lock-in amplifier for isolation of the photocurrent signal.

AC Photocurrent Measurement: Samples were held at a constant bias of 100 mV by a DC power supply. Contact was made to the EG device under test by two tungsten probes, with the outgoing signal delivered to a current preamplifier and SRS SR830 lock-in amplifier to isolate the photocurrent signal. The EG mesa under test was illuminated by a 444 nm diode laser (continuous wave power of 168 μw, rms power of 75

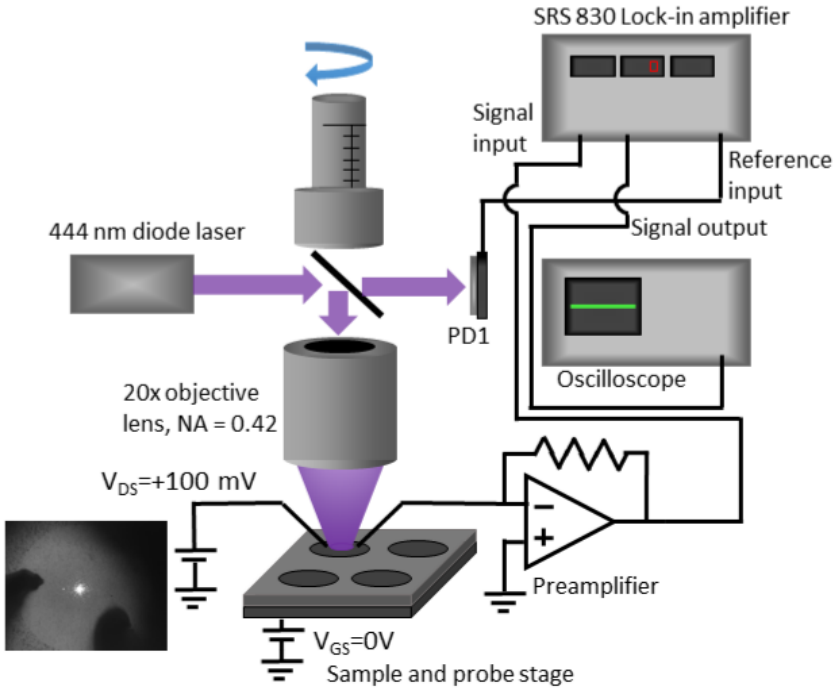

Figure 3.8: AC photocurrent measurement schematic. Illustration of the AC photocurrent measurement setup. A single lock-in amplifier was used to isolate the photocurrent signal.

μW) pulsed at a frequency of 37 Hz. The illumination area of the laser was defined by a circular spot size 50 μm in diameter. The dark current (resistance) was measured with a Keithley 2636A Source Meter Unit at DC prior to measurement of the AC photocurrent.

The magnitude signal was recorded as a function of time on a Digilent Analog Discovery module in oscilloscope mode.

AC Photoconductance Measurement: Samples were biased by the internal oscillator in a Signal Recovery lock-in amplifier at a frequency of 1 kHz and amplitude of 1 V rms; this AC bias was divided on a voltage divider with a DC bias of 100 mV to

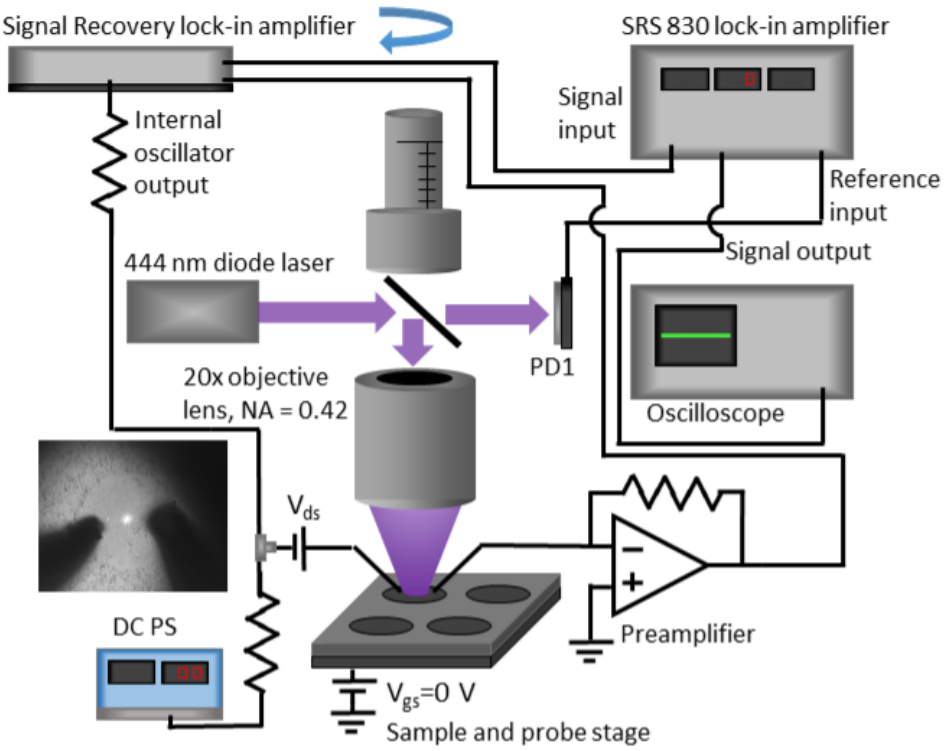

Figure 3.9: AC photoconductance measurement schematic. Illustration of the AC photoconductance measurement setup. A dual lock-in amplifier setup was used to modulate the applied bias and illumination frequencies.

yield an input voltage of 91 mV rms to the drain terminal. Contact was made to the EG device under test by two tungsten probes. The EG mesa under test was illuminated by a 444 nm diode laser (continuous wave power of 168 μw, rms power of 75 μW) pulsed at a frequency of 37 Hz. The outbound photoconductance signal was isolated by a current preamplifier, Signal Recovery lock-in amplifier, and SRS SR830 lock-in amplifier. The

magnitude signal was recorded as a function of time on a Digilent Analog Discovery module in oscilloscope mode.

CHAPTER 4: INTENSITY MODULATED PHOTOCURRENT SPECTROSCOPY OF AN EPITAXIAL GRAPHENE/SILICON CARBIDE BIPOLAR JUNCTION PHOTOTRANSISTOR

4.1: INTRODUCTION

As indicated previously, standalone EG/SiC devices can function as UV photodetectors.[2–4] For example, vertical bipolar junction phototransistors (BJTs) with an EG/p-SiC/n^+-SiC architecture were the subject of study in previous reports by Barker et al. and Chava et al. and are the focus of this chaper.[2,31] In brief, the EG, p-doped SiC epilayer, and n^+-SiC substrate functioned as the emitter, base, and collector, respectively, as shown in **Figure 4.1A**. Under bias, the device operated in two modes, as follows. Schottky emitter (SE) mode was defined by holding the EG at a negative bias with respect to the n^+-SiC substrate. Under such conditions, photogenerated holes in the epilayer base were repelled from migration to the EG by the p-type EG/p-SiC Schottky barrier; electrons were then injected from the EG and swept into the n^+-SiC to maintain charge, resulting in gain.[2] Schottky collector (SC) mode was defined by holding the EG at a positive bias with respect to the n^+-SiC substrate. Under such conditions, the bipolar gain mechanism was not present, and much lower photocurrents were reported. The device demonstrated high UV responsivity of ~7 A/W due to the bipolar gain mechanism in SE mode.[2] Energy band diagrams for the EG/SiC device under both operating modes are illustrated in **Figure 4.1B,C**.

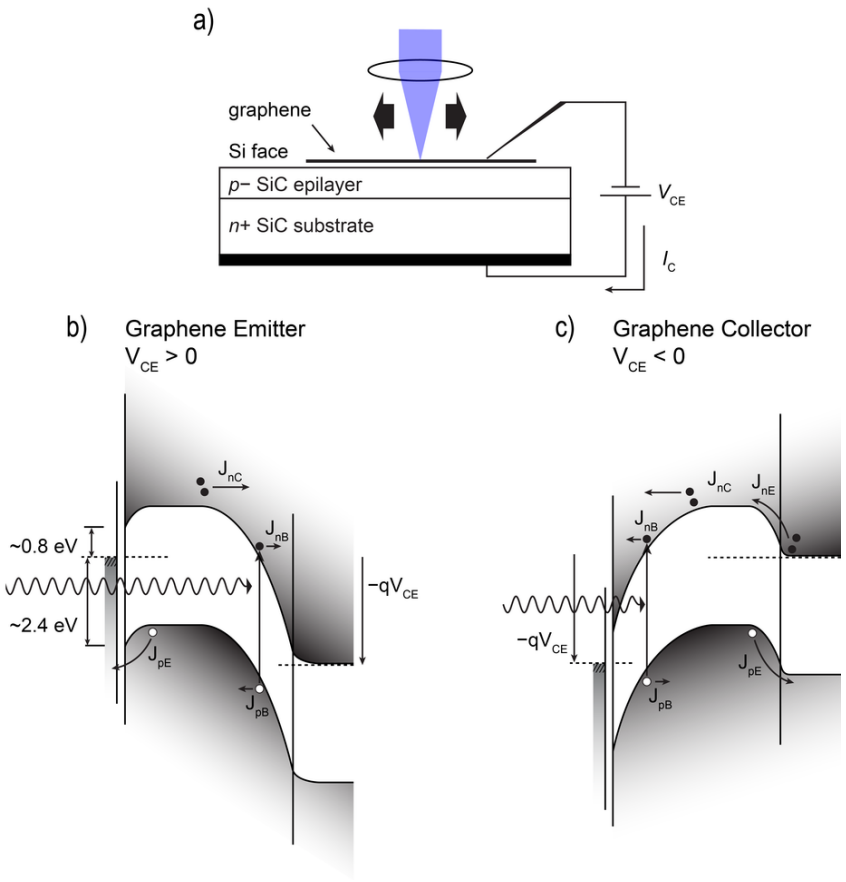

Figure 4.1: Probing configuration and energy band diagrams for the EG/SiC BJT. Panel A shows the probing configuration of the device in SE mode, with V_{CE} and I_C representing the collector-emitter voltage and the collector current, respectively. Panels B and C show the energy band diagrams of the device under illumination in SE and SC modes, respectively.

Although the sub-bandgap response of the device was well characterized and examined by SPCM, a few details of the localized device response remained unclear.[2] Specifically, in SE mode we observed a localized photocurrent under visible excitation (444 nm, 0.776 mW, chopped at a frequency of 287 Hz) at the edge of the EG mesa under test, and an accompanying roll-off in signal as the distance from the mesa edge increased; a representative SPCM map and accompanying photocurrent trace demonstrating this phenomena is displayed in **Figure 4.2A**. Because SPCM is an AC measurement with modulated illumination, measured signals are sensitive to attenuation

by resistor-capacitor (RC) delays. We hypothesized that this distinct roll-off could have originated from a characteristic RC phase delay off the edge of the EG in SE mode. In fact, the relative phase map obtained simultaneously with the photocurrent map of the device in SE mode indicated that the phase drifted to successively lower values from the edge of the mesas as expected for an increasing RC delay, as shown in **Figure 4.2B**.

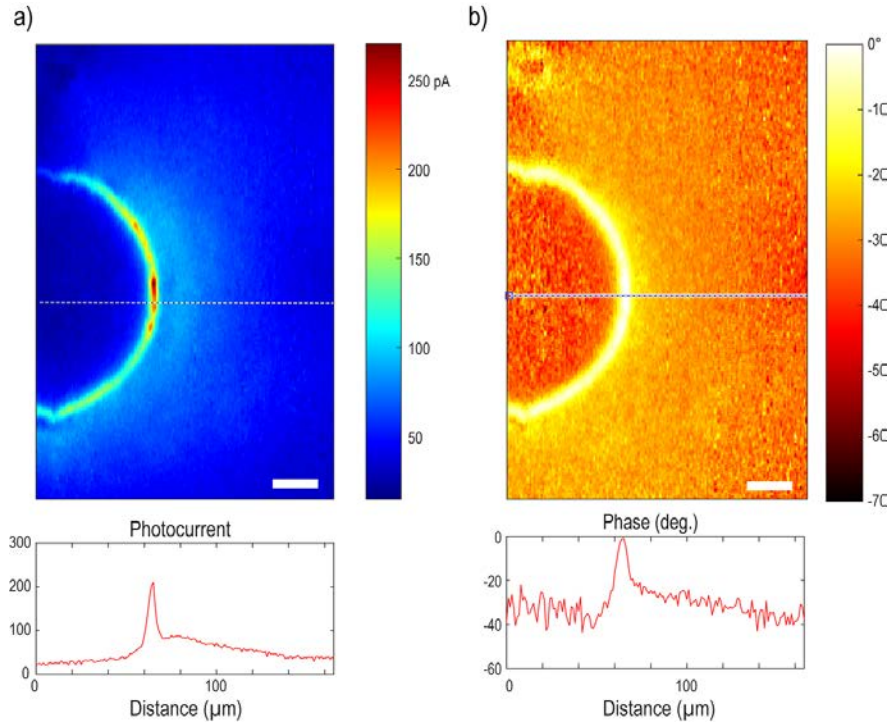

Figure 4.2: AC photocurrent and relative phase maps of the EG/SiC BJT Panel A shows a photocurrent map of a device in SE mode. Panel B shows the relative phase of the same device, with the phase zeroed at 0° on the edge of the EG mesa. Lower panels indicate profile traces corresponding to the dotted lines in panels A and B. the illumination source (444 nm, 0.776 mW) was chopped at a frequency of 287 Hz.

To further probe the origin of the phase delay observed in SPCM measurements as well as better understand the frequency response of the device, we chose to employ Intensity Modulated Photocurrent Spectroscopy (IMPS) experiments, as follows.

4.2: IMPS EXPERIMENT AND CONCLUSION

EG/SiC chip DH-20 served as the BJT for all of the work described herein. For all IMPS measurements, the device under test was held at a constant bias of 20 V in SE mode. The device under test was illuminated by UV (370 nm) and visible (444 nm) light sources modulated by a mechanical chopper. Both local and wide area illumination IMPS measurements were obtained, and the photocurrent and accompanying phase signals were recorded simultaneously. Local and wide area I-V characteristics were also obtained

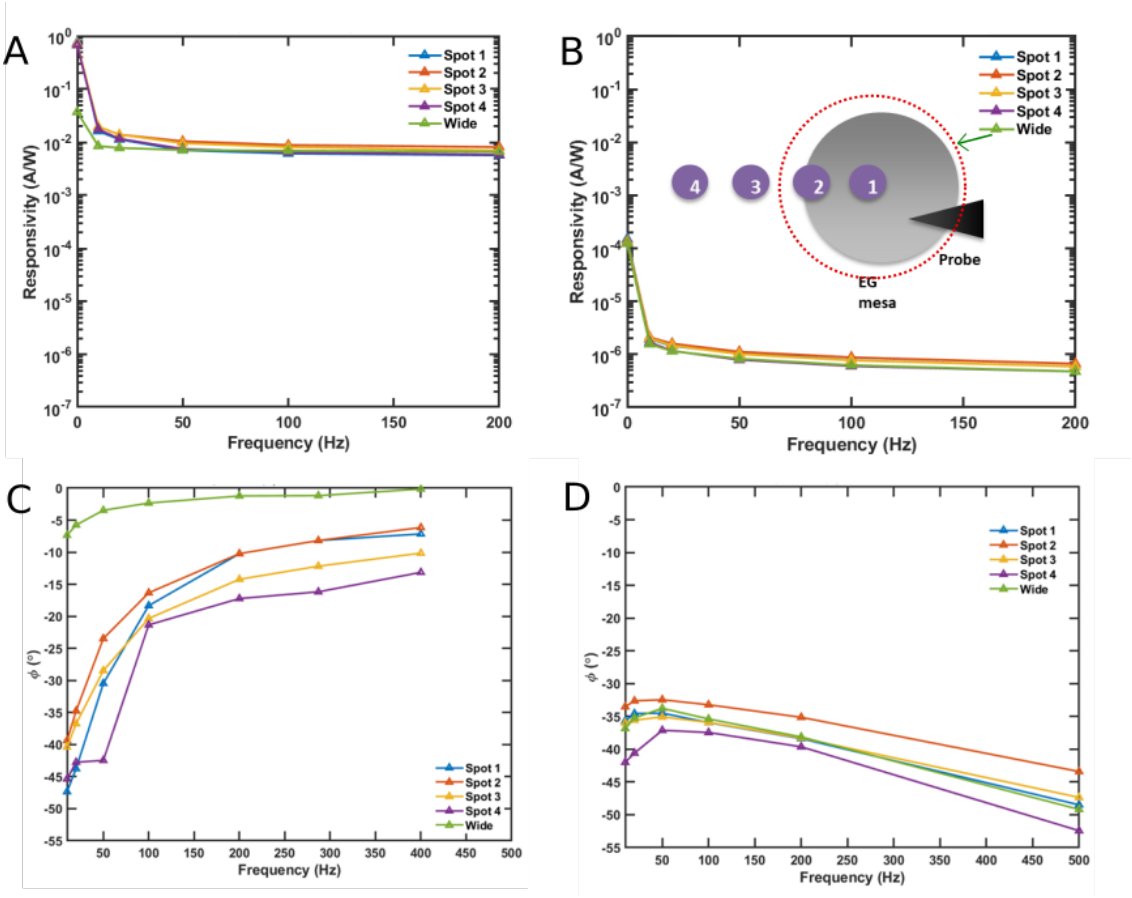

Figure 4.3: EG/SiC Bode plot and phase delay from IMPS characterization. Panel A and B show the responsivities obtained as a function of modulation frequency for UV (370 nm) and visible (444 nm) excitation, respectively. Phase angles recorded simultaneously with the data in Panels A and B are displayed in panels C and D; panel C and D reflect phase angles obtained from UV (370 nm) and visible (444 nm) excitation, respectively.

without modulated illumination to obtain the DC responsivities. As shown in **Figure 4.1A,B**, the responsivity of the device for all localized and wide area measurements was attenuated from DC (0 Hz) to AC (modulated). It is possible that this may be attributed to the slow speed of the device, as photocurrent rise times were ~46 ms. The graphic inset in **Figure 4.1B** shows the locations of each of the four spots used for IMPS measurements; the wide area illumination spot is also illustrated. We observed that all of the phase angles were negative, which was consistent with behavior stemming from a capacitive delay. Phase data for IMPS measurements under UV and visible excitation are shown in **Figure 4.1C,D**. We note that the phase varies non-monotonically with frequency in some cases. Although the exact origin of this phenomena is unknown, we conclude that such behavior may indicate that the phase delay originates from more than one characteristic frequency within the device.

4.3: EXPERIMENTAL

IMPS: For IMPS measurements, the device under test was biased at a constant bias of 20 V in Schottky Emitter mode by a Keithley 2636A Source Meter Unit.[2] For wide area IMPS measurements, the device was illuminated such that the entire EG mesa and surrounding edge was held incident with the light beam. The locations of spots 1-4 for localized IMPS measurements held a center-to-center spacing of 90 μm. The illumination beam was modulated by a mechanical chopper. The modulated photocurrent signal was delivered to an Ithaco 1211 current preamplifier and Stanford Research Systems SR830 lock-in amplifier for simultaneous isolation of the photocurrent and phase signals. The AC responsivity of the device was obtained using the calculation described in Chapter 3.

Current-voltage characteristic: Routine I-V measurements were taken using a Keithley 2636A Source Meter Unit to obtain the responsivity at DC (unmodulated illumination). EG/SiC chip DH-20 was used for the BJT experiments. Electrical contacts were made with a tungsten probe on the EG mesa under test, and Cu tape affixed to the bottom of the chip.

REFERENCES

(1) Li, X.; Zhu, H. The Graphene–Semiconductor Schottky Junction. *Physics Today* **2016**, *69* (9), 46–51. https://doi.org/10.1063/PT.3.3298.

(2) Barker, B. G.; Chava, V. S. N.; Daniels, K. M.; Chandrashekhar, M. V. S.; Greytak, A. B. Sub-Bandgap Response of Graphene/SiC Schottky Emitter Bipolar Phototransistor Examined by Scanning Photocurrent Microscopy. *2D Mater.* **2018**, *5* (1), 011003. https://doi.org/10.1088/2053-1583/aa90b1.

(3) Chava, V. S. N.; Omar, S. U.; Brown, G.; Shetu, S. S.; Andrews, J.; Sudarshan, T. S.; Chandrashekhar, M. V. S. Evidence of Minority Carrier Injection Efficiency >90% in an Epitaxial Graphene/SiC Schottky Emitter Bipolar Junction Phototransistor for Ultraviolet Detection. *Appl. Phys. Lett.* **2016**, *108* (4), 043502. https://doi.org/10.1063/1.4940385.

(4) Yang, J.; Guo, L.; Guo, Y.; Hu, W.; Zhang, Z. Epitaxial Graphene/SiC Schottky Ultraviolet Photodiode with Orders of Magnitude Adjustability in Responsivity and Response Speed. *Appl. Phys. Lett.* **2018**, *112* (10), 103501. https://doi.org/10.1063/1.5019435.

(5) Sze, S. M. *Physics of Semiconductor Devices*, 2nd ed.; Wiley, 1988.

(6) Saran, R.; Curry, R. J. Lead Sulphide Nanocrystal Photodetector Technologies. *Nat Photon* **2016**, *10* (2), 81–92. https://doi.org/10.1038/nphoton.2015.280.

(7) Moreels, I.; Lambert, K.; Smeets, D.; De Muynck, D.; Nollet, T.; Martins, J. C.; Vanhaecke, F.; Vantomme, A.; Delerue, C.; Allan, G.; et al. Size-Dependent Optical Properties of Colloidal PbS Quantum Dots. *ACS Nano* **2009**, *3* (10), 3023–3030. https://doi.org/10.1021/nn900863a.

(8) Zhang, J.; Crisp, R. W.; Gao, J.; Kroupa, D. M.; Beard, M. C.; Luther, J. M. Synthetic Conditions for High-Accuracy Size Control of PbS Quantum Dots. *J. Phys. Chem. Lett.* **2015**, *6* (10), 1830–1833. https://doi.org/10.1021/acs.jpclett.5b00689.

(9) Talapin, D. V.; Lee, J.-S.; Kovalenko, M. V.; Shevchenko, E. V. Prospects of Colloidal Nanocrystals for Electronic and Optoelectronic Applications. *Chem. Rev.* **2010**, *110* (1), 389–458. https://doi.org/10.1021/cr900137k.

(10) Sablon, K. A.; Sergeev, A.; Najmaei, S.; Dubey, M. High-Response Hybrid Quantum Dots- 2D Conductor Phototransistors: Recent Progress and Perspectives. *Nanophotonics* **2017**, *6* (6), 1263–1280. https://doi.org/10.1515/nanoph-2016-0159.

(11) Shen, Y.; Gee, M. Y.; Tan, R.; Pellechia, P. J.; Greytak, A. B. Purification of Quantum Dots by Gel Permeation Chromatography and the Effect of Excess Ligands on Shell Growth and Ligand Exchange. *Chem. Mater.* **2013**, *25* (14), 2838–2848. https://doi.org/10.1021/cm4012734.

(12) Zhitomirsky, D.; Voznyy, O.; Hoogland, S.; Sargent, E. H. Measuring Charge Carrier Diffusion in Coupled Colloidal Quantum Dot Solids. *ACS Nano* **2013**, *7* (6), 5282–5290. https://doi.org/10.1021/nn402197a.
(13) Guglietta, G. W.; Diroll, B. T.; Gaulding, E. A.; Fordham, J. L.; Li, S.; Murray, C. B.; Baxter, J. B. Lifetime, Mobility, and Diffusion of Photoexcited Carriers in Ligand-Exchanged Lead Selenide Nanocrystal Films Measured by Time-Resolved Terahertz Spectroscopy. *ACS Nano* **2015**, *9* (2), 1820–1828. https://doi.org/10.1021/nn506724h.
(14) Weidman, M. C.; Beck, M. E.; Hoffman, R. S.; Prins, F.; Tisdale, W. A. Monodisperse, Air-Stable PbS Nanocrystals via Precursor Stoichiometry Control. *ACS Nano* **2014**, *8* (6), 6363–6371. https://doi.org/10.1021/nn5018654.
(15) Konstantatos, G.; Badioli, M.; Gaudreau, L.; Osmond, J.; Bernechea, M.; de Arquer, F. P. G.; Gatti, F.; Koppens, F. H. L. Hybrid Graphene-Quantum Dot Phototransistors with Ultrahigh Gain. *Nat Nano* **2012**, *7* (6), 363–368. https://doi.org/10.1038/nnano.2012.60.
(16) Klem, E. J. D.; Shukla, H.; Hinds, S.; MacNeil, D. D.; Levina, L.; Sargent, E. H. Impact of Dithiol Treatment and Air Annealing on the Conductivity, Mobility, and Hole Density in PbS Colloidal Quantum Dot Solids. *Appl. Phys. Lett.* **2008**, *92* (21), 212105. https://doi.org/10.1063/1.2917800.
(17) Piliego, C.; Protesescu, L.; Bisri, S. Z.; Kovalenko, M. V.; Loi, M. A. 5.2% Efficient PbS Nanocrystal Schottky Solar Cells. *Energy Environ. Sci.* **2013**, *6* (10), 3054–3059. https://doi.org/10.1039/C3EE41479E.
(18) Bin, S.; Voznyy, O.; Tan, H.; Stadler, P.; Liu, M.; Walters, G.; Proppe, A. H.; Liu, M.; Fan, J.; Zhuang, T.; et al. Pseudohalide-Exchanged Quantum Dot Solids Achieve Record Quantum Efficiency in Infrared Photovoltaics - Sun - 2017 - Advanced Materials - Wiley Online Library. *Advanced Materials* **2017**, *29* (27), 1700749. https://doi.org/10.1002/adma.201700749.
(19) Bessonov, A. A.; Allen, M.; Liu, Y.; Malik, S.; Bottomley, J.; Rushton, A.; Medina-Salazar, I.; Voutilainen, M.; Kallioinen, S.; Colli, A.; et al. Compound Quantum Dot–Perovskite Optical Absorbers on Graphene Enhancing Short-Wave Infrared Photodetection. *ACS Nano* **2017**, *11* (6), 5547–5557. https://doi.org/10.1021/acsnano.7b00760.
(20) Kroupa, D. M.; Vörös, M.; Brawand, N. P.; McNichols, B. W.; Miller, E. M.; Gu, J.; Nozik, A. J.; Sellinger, A.; Galli, G.; Beard, M. C. Tuning Colloidal Quantum Dot Band Edge Positions through Solution-Phase Surface Chemistry Modification. *Nature Communications* **2017**, *8*, 15257. https://doi.org/10.1038/ncomms15257.
(21) Hwang, D. K.; Lee, Y. T.; Lee, H. S.; Lee, Y. J.; Shokouh, S. H.; Kyhm, J.; Lee, J.; Kim, H. H.; Yoo, T.-H.; Nam, S. H.; et al. Ultrasensitive PbS Quantum-Dot-Sensitized InGaZnO Hybrid Photoinverter for near-Infrared Detection and Imaging with High Photogain. *NPG Asia Mater* **2016**, *8* (1), e233. https://doi.org/10.1038/am.2015.137.
(22) Lin, Y.-M.; Dimitrakopoulos, C.; Jenkins, K. A.; Farmer, D. B.; Chiu, H.-Y.; Grill, A.; Avouris, P. 100-GHz Transistors from Wafer-Scale Epitaxial Graphene. *Science* **2010**, *327* (5966), 662–662. https://doi.org/10.1126/science.1184289.

(23) Davydov, S. Y.; Lebedev, A. A.; Posrednik, O. V. Estimation of the Energy Characteristics of the 3C-SiC/2H-, 4H-, 6H-, and 8H-SiC Heterojunctions. *Semiconductors* **2005**, *39* (12), 1391–1393. https://doi.org/10.1134/1.2140310.
(24) Singh, A.; Uddin, M. A.; Sudarshan, T.; Koley, G. Tunable Reverse-Biased Graphene/Silicon Heterojunction Schottky Diode Sensor. *Small* **2014**, *10* (8), 1555–1565. https://doi.org/10.1002/smll.201302818.
(25) Chen, C.-C.; Aykol, M.; Chang, C.-C.; Levi, A. F. J.; Cronin, S. B. Graphene-Silicon Schottky Diodes. *Nano Lett.* **2011**, *11* (5), 1863–1867. https://doi.org/10.1021/nl104364c.
(26) Zarghami, M. H.; Liu, Y.; Gibbs, M.; Gebremichael, E.; Webster, C.; Law, M. P-Type PbSe and PbS Quantum Dot Solids Prepared with Short-Chain Acids and Diacids. *ACS Nano* **2010**, *4* (4), 2475–2485. https://doi.org/10.1021/nn100339b.
(27) Nomani, M. W. K.; Shields, V.; Tompa, G.; Sbrockey, N.; Spencer, M. G.; Webb, R. A.; Koley, G. Correlated Conductivity and Work Function Changes in Epitaxial Graphene. *Appl. Phys. Lett.* **2012**, *100* (9), 092113. https://doi.org/10.1063/1.3691628.
(28) Davydov, S. Y. On the Electron Affinity of Silicon Carbide Polytypes. *Semiconductors* **2007**, *41* (6), 696–698. https://doi.org/10.1134/S1063782607060152.
(29) Robin, A.; Lhuillier, E.; Xu, X. Z.; Ithurria, S.; Aubin, H.; Ouerghi, A.; Dubertret, B. Engineering the Charge Transfer in All 2D Graphene-Nanoplatelets Heterostructure Photodetectors. *Scientific Reports* **2016**, *6*, 24909. https://doi.org/10.1038/srep24909.
(30) Reshanov Sergey A.; Emtsev Konstantin V.; Speck Florian; Gao Kun-Yuan; Seyller Thomas K.; Pensl Gerhard; Ley Lothar. Effect of an Intermediate Graphite Layer on the Electronic Properties of Metal/SiC Contacts. *physica status solidi (b)* **2008**, *245* (7), 1369–1377. https://doi.org/10.1002/pssb.200844083.
(31) Chava, V. S. N.; Barker, B. G.; Balachandran, A.; Khan, A.; Simin, G.; Greytak, A. B.; Chandrashekhar, M. V. S. High Detectivity Visible-Blind SiF4 Grown Epitaxial Graphene/SiC Schottky Contact Bipolar Phototransistor. *Appl. Phys. Lett.* **2017**, *111* (24), 243504. https://doi.org/10.1063/1.5009003.

APPENDIX A: EG/SiC CHIP INFORMATION

Table A.1: EG/SiC Chip Information

Sample ID	Information
DH-46	Blanket EG on SiC, sample was used with GPC-purified PbS QDs (1S: 945 nm/1.3 eV) for establishing film formation protocols
DH-48	Chip used for the barristor prototype. EG/n-SiC/n^+-SiC, mesa-isolated EG, TFS growth, n-epi 1.62×10^{14} cm^{-3}, 26µm thickness, sample was used with GPC-purified PbS QDs (1S: 1298 nm/0.95 eV), 13-15 ML EG.
CL-X3	Chip used for the photovoltage field-effect transistor. EG/n-SiC/n^+-SiC, mesa-isolated EG, TFS growth, n-epi 2×10^{16} cm^{-3}, 6µm thickness, 13-15 ML EG, sample was used with GPC-purified PbS QDs (1S: 945 nm/1.3 eV), 13-15 ML EG
DH-20	Chip used for the BJT. EG/p-SiC/n^+-SiC, mesa-isolated EG, TFS growth, p-epi 3.7×10^{14} cm^{-3}, 12.8µm thickness, 2-3 ML EG